Water Resources Research

RESEARCH ARTICLE
10.1029/2022WR033059

Under What Conditions Does Transverse Macrodispersion Exist in Groundwater Flow?

Daniel R. Lester[1], Marco Dentz[2], Prajwal Singh[3], and Aditya Bandopadhyay[3]

[1]School of Engineering, RMIT University, Melbourne, VIC, Australia, [2]Spanish National Research Council (IDAEA-CSIC), Barcelona, Spain, [3]Indian Institute of Technology Kharagpur (IITK), Kharagpur, India

Key Points:

- We prove that the transverse macrodispersion does not exist when the hydraulic conductivity field is smooth and locally isotropic
- We show that conventional numerical methods do not preserve this constraint, and propose novel numerical methods that do
- These insights reconcile previous contradictory results and question the ability of some conductivity models to represent real porous media

Correspondence to:
D. R. Lester,
daniel.lester@rmit.edu.au

Citation:
Lester, D. R., Dentz, M., Singh, P., & Bandopadhyay, A. (2023). Under what conditions does transverse macrodispersion exist in groundwater flow? *Water Resources Research*, *59*, e2022WR033059. https://doi.org/10.1029/2022WR033059

Received 21 JUN 2022
Accepted 3 MAR 2023

Abstract In recent years there has been vigorous debate whether asymptotic transverse macrodispersion exists in steady three-dimensional (3D) groundwater flows in the purely advective limit. This question is tied to the topology of 3D flow paths (termed the *Lagrangian kinematics*), specifically whether streamlines can undergo braiding motions or can wander freely in the transverse direction. In this study we determine which Darcy flows do admit asymptotic transverse macrodispersion for purely advective transport on the basis of the conductivity structure. We prove that porous media with smooth, locally isotropic hydraulic conductivity exhibit zero transverse macrodispersion under pure advection due to constraints on the Lagrangian kinematics of these flows, whereas either non-smooth or locally anisotropic conductivity fields can generate transverse macrodispersion. This has implications for upscaling locally isotropic porous media to the block scale as this can result in a locally anisotropic conductivity, leading to non-zero macrodispersion at the block scale that is spurious in that it does not arise for the fully resolved Darcy scale flow. We also show that conventional numerical methods for computation of particle trajectories do not explicitly preserve the kinematic constraints associated with locally isotropic Darcy flow, and propose a novel psuedo-symplectic method that preserves these constraints. These results provide insights into the mechanisms that govern transverse macrodispersion in groundwater flow, and unify seemingly contradictory results in the literature in a consistent framework. These insights call into question the ability of smooth, locally isotropic conductivity fields to represent flow and transport in real heterogeneous porous media.

Plain Language Summary The spreading of solutes, colloids and pollutants in groundwater flow is key to both risk assessment and a fundamental understanding of chemical, biological and geophysical transport in the subsurface. In many scenarios the spreading of solutes transverse to the mean flow direction is dominated by hydrodynamic transport from diverging streamlines and the contribution from local dispersion is relatively small. Although it is well understood that such hydrodynamic transport (termed transverse macrodispersion) is zero in steady two-dimensional groundwater flow for purely advective transport, there has been much debate in recent years as to whether transverse macrodispersion can occur in steady three-dimensional groundwater flows. In this study we address this question by considering the kinematics associated with Darcy flow of heterogeneous porous with different conductivity structures and identify the structures that generate non-zero transverse macrodispersion in the absence of local dispersion. We show that numerical predictions of transverse macrodispersion can be highly sensitive to the details of the numerical solvers used and propose a novel numerical method to mitigate against spurious predictions of transverse macrodispersion. These findings are used to reconcile seemingly contradictory results in the literature and provide insights into the suitability of commonly used models of groundwater flow and transport.

1. Introduction

The spreading of solutes, colloids and pollutants in groundwater flow is a key transport process that is central to a wide range of chemical, biological and geophysical processes in the subsurface. For instance, the transverse dispersion of pollutants and toxic solutes plays a critical role in risk assessment and hazard analysis, whereas transverse dispersion is fundamental to remediation of contaminated soils. Similarly, transverse dispersion of nutrients and organic species are central to the health of ecosystems and groundwater quality. This transport process is the only mechanism that reduces the concentration within the core of a steady plume (Domenico & Palciauskas, 1982), and the only means for compounds within a steady plume that can mix and thus react with surrounding compounds (Bauer et al., 2008; Cirpka et al., 2012). Hence, correct understanding, prediction and

quantification of transverse macrodispersion in groundwater flows is critical to understanding these processes in groundwater flows.

After a sufficient development period that is characterized by non-Fickian transport, the dispersion and transport of a solute plume at the Darcy scale in heterogeneous porous media behaves in a Fickian manner, and so may be described in terms of a large-scale (macroscopic) advection-dispersion equation (ADE). In this regime, transport is characterized by the associated macrodispersion tensor, which is anisotropic due to differential coupling between local dispersion and fluid advection. Although longitudinal dispersion dictates breakthrough characteristics of solutes and colloids, transverse macrodispersion is a controlling factor in transport and mixing in many applications.

In heterogeneous porous media, transverse macrodispersion is comprised of contributions from both fluid advection (also termed hydrodynamic dispersion) and local dispersion, and in many applications the contribution from the former is dominant. Significant progress has been made on understanding transverse macrodispersion in this limit in two-dimensional (2D) groundwater flow. Gelhar and Axness (1983) used first order perturbation theory to show that asymptotic transverse macrodispersion is of the order of pore-scale dispersion. Extension to fourth-order perturbation (Dagan, 1994) and eventually exact analysis (Attinger et al., 2004) subsequently showed that the hydrodynamic contribution to transverse macrodispersion is zero in steady 2D groundwater flow in the absence of local dispersion. This absence of transverse macrodispersion can be directly attributed to the presence of an analytic streamfunction for all divergence-free steady 2D flows. In this case the 1D streamlines of the flow are bound by neighboring streamlines in the 2D plane and so cannot diverge without bound, thus precluding transverse macrodispersion for purely advective transport.

Conversely, several theoretical (Attinger et al., 2004; Gelhar & Axness, 1983) and numerical (Beaudoin & de Dreuzy, 2013; Janković et al., 2003, 2009; Schwarze et al., 2001) studies have consistently found that asymptotic transverse macrodispersion is finite in steady three-dimensional (3D) groundwater flows. This marked difference with respect to 2D flow can be attributed to freedom of 1D streamlines in three spatial dimensions; as streamlines are now no longer confined to the 2D plane, they may move freely throughout the flow domain and so diverge without bound, leading to non-zero transverse macrodispersion in the purely advective limit.

However, closer consideration shows that some models of groundwater flow impose significant constraints (termed kinematic constraints) on the geometric structure of the streamlines of steady 3D flow. These constraints have significant implications for transport processes such as transverse macrodispersion, and the connection between flow topology and transport processes has been the focus of several research papers (de Barros et al., 2012; Chiogna et al., 2015; Cirpka et al., 2015) in the past decade. Recently, Lester et al. (2021) found that one commonly used model for groundwater flow, steady Darcy flow in porous media with a locally isotropic hydraulic conductivity field, constrains the transverse macrodispersivity to be zero in the case of purely advective transport, which is in conflict with the findings of previous studies (Attinger et al., 2004; Beaudoin & de Dreuzy, 2013; Cirpka et al., 2015; Gelhar & Axness, 1983; Janković et al., 2003, 2009; Schwarze et al., 2001). Given the importance of transverse macrodispersion to chemical and biological processes in groundwater flows, it is critical that these differences are reconciled and a clear understanding is developed regarding the conditions under which groundwater models admit finite transverse macrodispersion for purely advective transport. As experimental observations have clearly established that transverse macrodispersion is finite in geological media (Dagan, 1989), it is important that groundwater flow models are employed that accurately quantify this critical transport mechanism. These insights are also relevant to solute transport in the non-Fickian pre-asymptotic regime, as these kinematic constraints impact transport at all times. However, for simplicity of exposition, in this study we shall focus mainly on the Fickian regime. Hence there is a general need to uncover the kinematics of various groundwater flow models and quantify the impact upon solute transport.

In this study we determine which commonly-used groundwater models admit transverse macrodispersion by consideration of the Lagrangian kinematics of these models. As these kinematics govern the streamlines of the flow, in this study we first consider the case of purely advective transport. It is important to first develop a complete understanding of these kinematics before consideration of their interplay with local dispersion. In Section 6 we consider the interaction of local dispersion and advection, and highlight the impact of Lagrangian kinematics upon macrodispersion. We also resolve discrepancies with previous studies by performing a detailed appraisal of commonly-used numerical methods for computation of transverse macrodispersion. We identify the classes of flow models which do and do not admit finite transverse macrodispersion and provide

a mathematical proof of zero transverse macrodispersion in the latter class. We also analyze numerical errors associated with conventional particle tracking methods and discuss the implications for accurate prediction of transverse macrodispersion. This study provides deep insights into the nature and origins of transverse macrodispersion in groundwater flow models, and highlights the precautions required to prevent spurious predictions of transverse macrodispersion in numerical simulations. Furthermore, as experimental studies (Dagan, 1989; Gelhar, 1993) show that all heterogeneous porous media exhibit non-zero transverse macrodispersion in the limit of large Peclét number, these findings call into question the ability of some classes of conductivity models to faithfully represent flow and transport in real heterogeneous porous media.

To simplify quantification of transverse dispersion, we consider the dispersion of a steady, continuously injected solute plume where concentration gradients along streamlines are negligible compared those transverse to streamlines. As longitudinal dispersion is absent under this scenario, nonlinear effects associated with the interplay between longitudinal and transverse dispersion are also absent. Although well documented (Dagan, 1994), this nonlinear mechanism is often overlooked and is typically small, leading to $\ln t$ growth of transverse variance when longitudinal dispersion is non-zero. As this mechanism does not lead to broadening of a non-diffusive solute plume at fixed longitudinal locations, this correction is not considered to contribute to transverse macrodispersion in this study.

The remainder of this manuscript is structured as follows. In Section 2 we briefly review the governing equations for the macrodispersion tensor in general groundwater flows. We consider the kinematics of commonly used groundwater flow models in Section 3, and in Section 4 we prove that transverse macrodispersion is zero for steady 3D isotropic Darcy flow. In Section 5 we consider errors associated with conventional numerical particle tracking methods in these flows and propose a novel particle tracking algorithm to rectify these errors. In Section 6 we develop models of transverse macrodispersion based upon the interactions between local dispersion and fluid deformation and compare model predictions with the numerical methods considered in Section 5. Finally, in Section 7 we summarize our findings and discuss implications for modeling of groundwater flow and transport.

2. Transverse Macrodispersion in Groundwater Flows

In this section we briefly review the macroscopic Fickian transport equations for the evolution of a solute plume at the Darcy scale in heterogeneous porous media and present the governing equations for the macrodispersion tensor components. We first consider the local-scale evolution of the concentration field $c(\mathbf{x}, t)$ of a solute plume with initial concentration $c_0(\mathbf{x})$ at time $t = 0$ in a steady porous media flow $\mathbf{v}(\mathbf{x})$ which is modeled via the ADE

$$\theta \frac{\partial c(\mathbf{x}, t)}{\partial t} + \nabla \cdot (\theta \mathbf{v}(\mathbf{x}) - \theta \mathbf{D}_0 \cdot \nabla) c(\mathbf{x}, t) = \theta c_0(\mathbf{x}) \delta(t), \tag{1}$$

where θ is the constant porosity of the aquifer and $\mathbf{D}_0$ is the constant local dispersion tensor. The steady groundwater velocity field $\mathbf{v}(\mathbf{x})$ is assumed to comprise of a mean field component in the $\hat{\mathbf{e}}_1$-direction, $\overline{\mathbf{v}} = \overline{v}\hat{\mathbf{e}}_1$, and the remaining fluctuation $\tilde{\mathbf{v}}(\mathbf{x})$ as

$$\mathbf{v}(\mathbf{x}) = \overline{\mathbf{v}} + \tilde{\mathbf{v}}(\mathbf{x}). \tag{2}$$

Upscaling of the local ADE (1) to the macroscale can be achieved via the Coarse Graining method (Beckie, 2001; Dykaar & Kitanidis, 1992; Rubin et al., 1999) which smooths local variables over the averaging volume $V(\mathbf{x})$ centered about the location $\mathbf{x}$ via the averaging procedure

$$\langle c(\mathbf{x}, t) \rangle \equiv \frac{1}{V(\mathbf{x})} \int_{\mathbf{y} \in V(\mathbf{y})} c(\mathbf{x} + \mathbf{y}, t) d^d \mathbf{y}. \tag{3}$$

Application of this averaging procedure to the local ADE (1) yields the macroscale transport equation (Attinger et al., 2004; Neuman & Zhang, 1990; Zhang & Neuman, 1990)

$$\theta \frac{\partial \langle c(\mathbf{x}, t) \rangle}{\partial t} + \theta \overline{\mathbf{v}} \cdot \nabla \langle c(\mathbf{x}, t) \rangle - \theta \nabla \cdot ((\mathbf{D}_0 + \mathbf{D}^m) \cdot \nabla \langle c(\mathbf{x}, t) \rangle) = 0, \tag{4}$$

where $\mathbf{D}^m$ is the constant macrodispersion tensor that quantifies the impact of unresolved subscale effects upon dispersion, whose elements are formally given by the Coarse Graining method as (Attinger et al., 2004; Bouchaud & Georges, 1990; McComb, 1990; Neuman, 1993)

$$D_{ij}^{m} \equiv \langle \tilde{v}_i \chi_j(\mathbf{x}) \rangle, \tag{5}$$

where the auxiliary fields $\chi_j(\mathbf{x})$ satisfy

$$(\mathbf{v}(\mathbf{x}) \cdot \nabla - \nabla \cdot \mathbf{D}_0 \cdot \nabla)\chi_j(\mathbf{x}) = \tilde{v}_j(\mathbf{x}), j = 1 : 3. \tag{6}$$

In many Darcy-scale applications the macroscale Pèclet number $\mathrm{Pe} = \overline{v}l/|\mathbf{D}_0|$ is large, where l is the correlation length-scale of the groundwater flow field $\mathbf{v}(\mathbf{x})$. Hence the PDE (6) governing the auxiliary fields $\chi_j(\mathbf{x})$ may be well approximated via the purely advective limit

$$\mathbf{v}(\mathbf{x}) \cdot \nabla \chi_j(\mathbf{x}) = \tilde{v}_j(\mathbf{x}), j = 1 : 3. \tag{7}$$

Hence the macrodispersion tensor computed using Equation 7 characterizes the contribution of purely hydrodynamic (advective) transport upon transverse macrodispersion in heterogeneous porous media. This formulation will be used in Section 4 to determine the transverse macrodispersion components D_{22}^{m}, D_{33}^{m} in a model groundwater flow.

3. Lagrangian Kinematics of Groundwater Flow

At the mesoscale ($\sim 10^{-1}$–10^{0} m), groundwater flow in heterogeneous porous media is typically modeled via the Darcy equation

$$\mathbf{v}(\mathbf{x}) = -\mathbf{K}(\mathbf{x}) \cdot \nabla \phi(\mathbf{x}), \quad \nabla \cdot \mathbf{v}(\mathbf{x}) = 0, \tag{8}$$

which represents an effective representation of mesoscale groundwater flow velocity $\mathbf{v}(\mathbf{x})$ resulting from of upscaling of Stokes flow at the pore-scale. Here $\phi(\mathbf{x})$ is the mean potential field (upscaled from the pore-scale pressure) and $\mathbf{K}(\mathbf{x})$ is the hydraulic conductivity tensor, the elements $K_{ij}(\mathbf{x})$ of which are typically modeled as random spatial variables with a prescribed correlation structure that are conditioned to given statistical parameters. In this study we assume that these random fields (and the associated potential and velocity fluctuations) are statistically stationary and ergodic, (meaning ensemble averages can be viably interchanged with spatial averages and vice-versa). The random fields $K_{ij}(\mathbf{x})$ may be either independent or correlated, and also may be statistically anisotropic with respect to their correlation structure in various spatial directions $\mathbf{x} = (x_1, x_2, x_3)$. The conductivity fields $K_{ij}(\mathbf{x})$ may also be non-smooth and contain impermeable regions (where $K_{ij} = 0$), but the conductivity is assumed to be everywhere finite.

The tensorial nature of the conductivity tensor arises from the grain structure of the porous medium at the pore scale (Bear, 1972). Many groundwater models of geological media assume locally isotropic hydraulic conductivity, where the components $K_{ij}(\mathbf{x})$ satisfy $K_{ij}(\mathbf{x}) = \delta_{ij}k(\mathbf{x})$. The scalar field $k(\mathbf{x})$ is simply known as the hydraulic conductivity field, and the anisotropic Darcy Equation 8 simplifies to its isotropic analog

$$\mathbf{v}(\mathbf{x}) = -k(\mathbf{x})\nabla \phi(\mathbf{x}), \quad \nabla \cdot \mathbf{v}(\mathbf{x}) = 0. \tag{9}$$

Note that locally isotropic porous media may also be statistically anisotropic in that the correlation structure of $k(\mathbf{x})$ is anisotropic, such statistical anisotropy is ubiquitous in unconsolidated geological media due to depositional processes (Bear, 1972). It is important to note that such locally isotropic yet statistically anisotropic media are still described by a scalar conductivity field as per Equation 9.

Although some studies (Chaudhuri & Sekhar, 2005; Dartois et al., 2018; Guin et al., 1972; Neuman et al., 1987) consider transverse macrodispersion in locally anisotropic porous media, the majority of studies (Attinger et al., 2004; Beaudoin & de Dreuzy, 2013; Chiogna et al., 2015; Cirpka et al., 2015; Dagan, 1987; Gelhar & Axness, 1983; Janković et al., 2003, 2009) consider isotropic porous media. Although classical studies (Dagan, 1987; Gelhar & Axness, 1983; Neuman & Zhang, 1990; Rubin & Gómez-Hernández, 1990) based on first order perturbation theory suggested transverse macrodispersion is zero in the purely advective limit, subsequent numerical and analytic studies have found that transverse macrodispersion is finite. A noteworthy case is that of Janković et al. (2003, 2009) who consider dispersion in an anisotropic medium with impermeable inclusions and so in this case the conductivity field is both non-smooth and has regions of zero conductivity. Schwarze et al. (2001) consider transverse macrodispersion in a synthetic random 3D velocity field that is generated by an approach similar to that proposed by Kraichnan (1961), rather than a solution of the Darcy equation. As this

velocity field is not explicitly helicity free, the topology of this flow field is akin to that of anisotropic Darcy flow. All of the above studies (involving anisotropic and isotropic Darcy flow) that extend beyond first-order perturbation theory find that transverse macrodispersion is finite, which is in accordance with experimental observations (Dagan, 1989). This finding makes intuitive sense as streamlines can wander freely in 3D heterogeneous media.

Despite this weight of evidence, it has recently been shown by Lester et al. (2021) that in the case of steady isotropic 3D Darcy flow with smooth, finite conductivity fields (and in the absence of stagnation points arising from e.g., flow boundaries and/or injection and extraction wells) that the geometry of the streamlines of these 3D groundwater flows is heavily constrained, which in turn impacts transverse macrodispersion. These constraints, which stem from the *Lagrangian kinematics* of the flow, arise because the helicity density $h(\mathbf{x})$, defined as the dot product between the flow velocity $\mathbf{v}(\mathbf{x})$ and vorticity $\boldsymbol{\omega}(\mathbf{x}) \equiv \nabla \times \mathbf{v}(\mathbf{x})$ is everywhere zero due to the identity

$$h(\mathbf{x}) \equiv \mathbf{v}(\mathbf{x}) \cdot \boldsymbol{\omega}(\mathbf{x}) = k \nabla \phi \cdot (\nabla k \times \nabla \phi) = 0. \tag{10}$$

The helicity H, defined as the volume integral of the helicity density $H = \int_{\Omega} h(\mathbf{x}) d^d\mathbf{x}$ over the flow domain Ω, is a measure of the *topological complexity* of a given flow (Moffatt, 1969; Moffatt & Tsinober, 1992; Moreau, 1961), in that the helicity measures quantities such as the knottedness of streamlines and the degree of braiding of streamlines as they move through the flow domain. The helicity-free condition (10), along with the stagnation-free condition

$$\mathbf{v}(\mathbf{x}) \neq \mathbf{0} \, \forall \mathbf{x} \in \Omega, \tag{11}$$

ensures that the streamlines of isotropic Darcy flows do not posses knots or braided structures.

In a series of pioneering studies, Sposito (1994, 1997, 2001) argued that the helicity-free property of isotropic Darcy flow led to the formation of 2D coherent *Lamb surfaces*, non-intersecting surfaces that are spanned by streamlines and vortex lines that foliate the flow domain. As streamlines are confined to these 2D coherent surfaces, the kinematics of isotropic Darcy flow is essentially 2D. However, subsequent investigation (Lester et al., 2019) showed that Lamb surfaces only exist for isotropic Darcy flows that are inherently 2D such as stratified media, and do not exist in general in steady 3D isotropic Darcy flow. This presented a conundrum as the helicity-free flows are well known to possess constrained Lagrangian kinematics (Holm & Kimura, 1991), but it was clear that these flows don't admit Lamb surfaces per se.

Lester et al. (2021) later showed that the helicity-free nature of steady 3D isotropic Darcy flows also ensures that they are *integrable* (in the dynamical systems sense (Arnol'd, 1997)), in that they posses two invariants (constants of motion), that we may term $\psi_1(\mathbf{x})$, $\psi_2(\mathbf{x})$ which do not vary along streamlines, and so satisfy

$$\mathbf{v}(\mathbf{x}) \cdot \nabla \psi_1(\mathbf{x}) = 0, \ \mathbf{v}(\mathbf{x}) \cdot \nabla \psi_2(\mathbf{x}) = 0. \tag{12}$$

Yoshida (2009) has shown that steady 3D flows that are helicity free can be expressed in terms of the Euler potentials (given by the curl of the Clebsch decomposition $\psi_1 \nabla \psi_2$), such that the velocity field may be represented as

$$\mathbf{v}(\mathbf{x}) = \nabla \psi_1(\mathbf{x}) \times \nabla \psi_2(\mathbf{x}), \quad \nabla \psi_1(\mathbf{x}) \neq \mathbf{0}, \nabla \psi_2(\mathbf{x}) \neq \mathbf{0}, \forall \mathbf{x}, \tag{13}$$

and so the invariants $\psi_1(\mathbf{x})$, $\psi_2(\mathbf{x})$ play the role of dual streamfunctions of the 3D flow (Bear, 1972; Greywall, 1993; Zijl, 1986). As shown in Figure 1a, the intersection of the level sets (2D streamsurfaces) of these streamfunctions gives rise to a 1D streamline that is defined as having constant (invariant) ψ_1, ψ_2 along its extent as shown in Equation 12.

Zijl (1986) show that these streamfunctions are governed by the coupled nonlinear elliptic partial differential equations

$$\nabla^2 \psi_1 - \nabla \ln k \cdot \nabla \psi_1 = S_2, \nabla^2 \psi_2 - \nabla \ln k \cdot \nabla \psi_2 = S_1, \tag{14}$$

where

$$S_i = \frac{(\mathbf{B} \times \nabla \psi_i) \cdot (\nabla \psi_1 \times \nabla \psi_2)}{|\nabla \psi_1 \times \nabla \psi_2|^2}, \quad \mathbf{B} \equiv (\nabla \psi_1 \cdot \nabla) \nabla \psi_2 - (\nabla \psi_2 \cdot \nabla) \nabla \psi_1.$$

Lester et al. (2021) demonstrate that solution of these equations yields the same velocity field as that given by solving the flow potential ϕ. Although the nonlinearities S_1, S_2 render these equations considerably more complex than that for ϕ, resolution of the streamfunctions bring significant benefits with respect to understanding and quantification of transport.

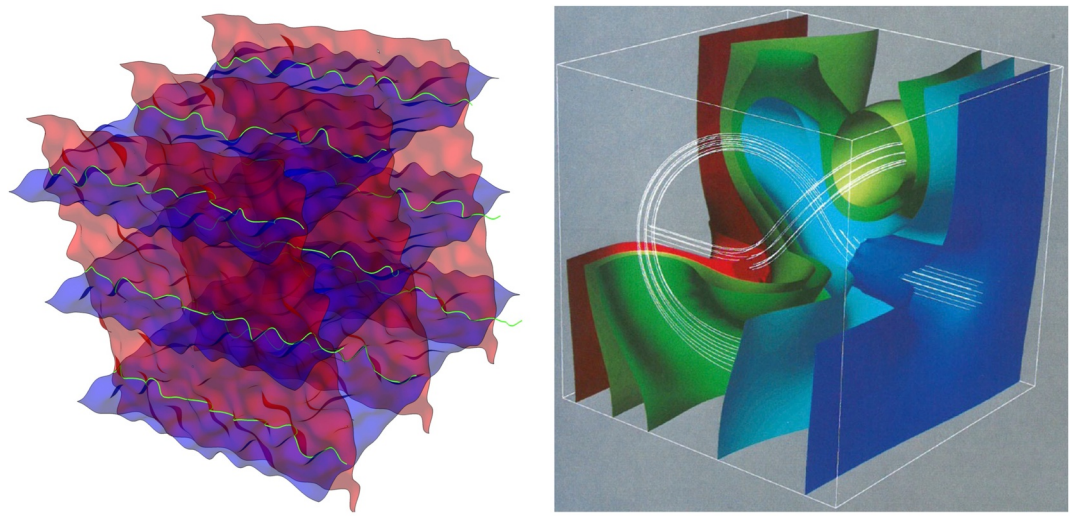

Figure 1. (a) Typical streamsurfaces (level sets) of streamfunctions $\psi_1(\mathbf{x})$ (blue) and $\psi_2(\mathbf{x})$ (red) for a steady heterogeneous isotropic 3D Darcy flow. Intersections of streamsurfaces form streamlines (green lines), hence streamfunctions ψ_1, ψ_2 are invariants of the flow. Adapted from Lester et al. (2021). (b) Knotted fluid particle trajectories (white lines) and associated isopotential surfaces in a steady anisotropic 3D Darcy flow. Here the tensorial nature of the conductivity field means this flow is not helicity-free, and so can admit a richer set of kinematics (such as the knotted flow structure shown) than isotropic Darcy flow. Adapted from Cole and Foote (1990).

It is important to note that in contrast to steady divergence-free 2D flows, not all steady divergence-free 3D flows admit the dual streamfunction representation (13). This can be readily demonstrated as all divergence-free flows can be expressed in terms of a vector potential $\mathbf{A}(\mathbf{x})$ as $\mathbf{v} = \nabla \times \mathbf{A}(\mathbf{x})$, and in turn, all 3D vector fields can be expressed in terms of generalized Clebsch potentials as

$$\mathbf{A}(\mathbf{x}) = \nabla\varphi(\mathbf{x}) + \sum_{i=1}^{M} \alpha_i(\mathbf{x})\nabla\beta_i(\mathbf{x}), \tag{15}$$

where the gradient potential φ is redundant due to the identity $\nabla \times \nabla\varphi = 0$. Yoshida (2009) shows that the conventional Clebsch decomposition (corresponding to $M = 1$ in Equation 15) is not sufficient to represent all steady 3D vector fields, but rather two ($M = 2$) or three ($M = 3$) pairs of Clebsch potentials are required, depending upon the boundary conditions of the flow field. An important exception, however is d-dimensional flows which are *integrable*, in that they possess $(d - 1)$ invariants (constants of motion) of the flow, in which case the conventional Clebsch decomposition ($M = 1$) is sufficient. This is exactly the case for helicity-free flows (Arnol'd, 1997) such as isotropic Darcy flow, in which case the streamfunctions of the flow are equivalent to the Clebsch potentials as $\psi_1 = \alpha_1$, $\psi_2 = \beta_1$. Thus, all steady 3D helicity-free flows admit the dual streamfunctions ψ_1, ψ_2.

The stagnation-free condition (11) ensures that the streamsurfaces (level sets of the streamfunctions) of the flow do not coincide as $\nabla\psi_1 \neq \mathbf{0}$, $\nabla\psi_2 \neq \mathbf{0}$. The stagnation-free condition holds for pressure-driven Darcy flows (Bear, 1972), but Darcy flows driven by source terms can admit stagnation points and thus interconnecting streamsurfaces at these stagnation points. Such interconnection raises the potential for violation of the kinematic constraints associated with the helicity-free condition, however such questions are beyond the scope of this study which is concerned with pressure-driven Darcy flows.

The existence of the two invariant streamfunctions $\psi_1(\mathbf{x})$, $\psi_2(\mathbf{x})$ simplifies the 3D advection equation for the position $\mathbf{x}(t)$ of a fluid tracer particle

$$\frac{d\mathbf{x}}{dt} = \mathbf{v}(\mathbf{x}(t)), \mathbf{x}(t = 0) = \mathbf{x}_0, \tag{16}$$

to the 1D integral

$$\frac{ds}{dt} = v(s; \psi_1(\mathbf{x}_0), \psi_2(\mathbf{x}_0)) \Rightarrow t(s) = \int_0^s \frac{1}{v(s; \psi_1(\mathbf{x}_0), \psi_2(\mathbf{x}_0))} ds, \tag{17}$$

where s is the distance traveled along a streamline with initial position $\mathbf{x} = \mathbf{x}_0$, and $v(s; \psi_1(\mathbf{x}_0), \psi_2(\mathbf{x}_0))$ is the magnitude of the fluid velocity magnitude along this streamline as a function of s.

As shown in Figure 1a, a given streamline is confined to reside within each of its associated 2D streamsurfaces (given by level sets of ψ_1 and ψ_2). Hence these streamlines experience the same type of constraints that arise for steady 2D flows in that they cannot cross neighboring streamlines within a given streamsurface. This means that like the 2D case, the transverse distance between a pair of streamlines can only fluctuate about a mean value as the streamlines navigate high and low permeability regions of the porous matrix, but cannot continually diverge without bound. This leads to the intuitive result that the streamlines of steady 3D Darcy flow can only fluctuate about a mean location in a 2D plane transverse to the mean flow direction and so these flows do not exhibit transverse macrodispersion. Lester et al. (2021) provide a mathematical argument as to why flows of the form (13) exhibit zero transverse macrodispersion, but in Section 4 we develop a rigorous mathematical proof of this result. Lester et al. (2022) also show that, due to their helicity-free nature, fluid deformation in steady 3D isotropic Darcy flow is very similar to that of steady 2D flows in general.

Conversely, Attinger et al. (2004) derived the exact result (i.e., not subject to perturbation truncation) that transverse macrodispersion in steady 3D isotropic Darcy flow groundwater flows is finite, as unlike steady 2D flow, 1D streamlines can wander freely throughout the 3D flow domain, leading to non-zero transverse macrodispersion. However, although this is true of steady 3D flows in general, this analysis did not account for the kinematic constraints associated with isotropic Darcy flow.

Conversely, groundwater flows that are not helicity-free do not admit the streamfunction representation (13). As explained below, these include locally anisotropic Darcy flow (as $h = \mathbf{K} \cdot \nabla\phi \cdot (\nabla \times (\mathbf{K} \cdot \nabla\phi)) \neq 0$ in general) (Chaudhuri & Sekhar, 2005; Dartois et al., 2018; Neuman et al., 1987), and isotropic Darcy flow with either non-smooth hydraulic conductivity k or stagnation points (Janković et al., 2003, 2009), in the flow. From Equation 13, the impact of a stagnation point is to locally render at least one of the streamfunction gradients $\nabla\psi_i$ to be zero, meaning that associated streams then intersect at this point, opening the possibility for transport between streamsurfaces and hence relaxation of the kinematic constraints associated with helicity-free flows. For the case of non-smooth conductivity fields, the velocity gradient is discontinuous over a discontinuity in the spatial conductivity gradient, hence the vorticity and helicity is ill-defined over this boundary. This discontinuity means that streamlines cannot be extended over this boundary via a Taylor series expansion as the associated velocity derivatives are discontinuous, and so the resultant streamlines are kinked. Associated with these velocity gradients is the helicity-free condition that places constraints on the velocity gradient (namely that $h \equiv \mathbf{v} \cdot (\boldsymbol{\varepsilon} : \nabla\mathbf{v}) = 0$, where $\boldsymbol{\varepsilon}$ is the Levi-Civita symbol), and so these kinematic constraints do not carry over this boundary. Although it is tempting to suggest that this discontinuity in spatial conductivity gradient can be smoothed over an arbitrarily small transition region, this smoothed case is fundamentally different in that the associated velocity field is now smooth and so the kinematic constraints associated with the helicity-free condition persist throughout the flow domain. In this sense, the case of a non-smooth hydraulic conductivity field represents a singular limit of a smooth but rapidly varying conductivity field.

Hence the above flows (i.e., those with stagnation points or locally anisotropic or non-smooth conductivity fields) are not *integrable* and so may exhibit complicated flow topology such as the knotted streamlines shown in Figure 1b that arise in numerical simulations (Cole & Foote, 1990) of anisotropic Darcy flow. Similarly, the non-stationary anisotropic Darcy flows considered by Chiogna et al. (2014); Chiogna et al. (2015) have non-zero helicity and show clear evidence of braiding of streamlines and accelerated mixing. Janković et al. (2009) show that such braiding is directly related to the generation of transverse macrodispersion, and demonstrate that isotropic but non-smooth conductivity fields can yield non-zero helicity in steady 3D Darcy flow. Thus, in the absence of confining streamfunctions ψ_1, ψ_2, the streamlines of general 3D steady flows can wander without bound throughout the flow domain, leading to complex flow topologies and non-zero transverse macrodispersion.

A noteworthy class of flows are those generated by heterogeneous porous media that is smooth and locally isotropic, but the correlation structure of the conductivity field is statistically anisotropic (Chiogna et al., 2015; Cirpka et al., 2015). Although more complicated than the flow depicted in Figure 1a, these statistically anisotropic flows are still helicity-free as the identity (10) still holds for these flows, and so they also admit a pair of

streamfunctions that constrain the Lagrangian kinematics in the same way as locally and statistically isotropic Darcy flows. Although the streamfunctions for statistically anisotropic Darcy flows are expected to be more complicated than those shown in Figure 1a, their existence alone is sufficient to ensure that these kinematic constraints still apply. Given the complexity of statistically anisotropic but locally isotropic flows, further care must be taken in analyzing transport in these flows to ensure this streamfunction structure and its impact on transport is preserved.

The arguments above reconcile the apparently contradictory results from theoretical studies as to whether transverse macrodispersion exists across various groundwater flow models. However, they do not explain discrepancies in the results from numerical studies, which require closer examination of conventional numerical methods for computation of transverse macrodispersion. In contrast to the theoretical results outlined above, several numerical studies (Beaudoin & de Dreuzy, 2013; Chiogna et al., 2015; Cirpka et al., 2015) also find that transverse macrodispersion is finite in steady isotropic 3D Darcy flow with a smooth and finite hydraulic conductivity field. These studies use particle tracking methods (given by solution of the advection Equation 16) to directly compute transverse macrodispersion. These particle tracking methods typically rely upon numerical approximations of the underlying velocity field which preserve the divergence of the true velocity field, but not necessarily the curl. However, specialized numerical methods are required to ensure that the kinematic constraints associated with the existence of the dual streamfunctions ψ_1, ψ_2 are rigorously enforced, and failure to do so can result in spurious predictions of transverse macrodispersion. This issue is explored in greater detail in Section 5, where the properties of conventional particle tracking methods such the Pollock algorithm (Pollock, 1988) and Runge-Kutta particle-tracking methods are examined in greater detail. However, before considering the issues associated with numerical particle tracking, it is necessary to first develop a rigorous proof that transverse macrodispersion is zero in isotropic Darcy flow.

4. Transverse Macrodispersion in Locally Isotropic Darcy Flow

To develop a mathematical proof of the result that transverse macrodispersion is zero in locally isotropic Darcy flow, we consider the streamfunctions of a steady state 3D isotropic Darcy flow in terms of their fluctuating and mean field components as

$$\psi_1(\mathbf{x}) = \overline{\psi}_1(\mathbf{x}) + \tilde{\psi}_1(\mathbf{x}) \qquad \psi_2(\mathbf{x}) = \overline{\psi}_2(\mathbf{x}) + \tilde{\psi}_2(\mathbf{x}). \tag{18}$$

For simplicity of exposition we consider the following mean streamfunctions that are aligned with the x_2, x_3 coordinates as

$$\overline{\psi}_1(\mathbf{x}) \equiv \overline{v} x_2, \overline{\psi}_2(\mathbf{x}) \equiv x_3, \tag{19}$$

which may be chosen as such due to non-uniqueness of the streamfunctions ψ_1, ψ_2 for a given velocity field (Lester et al., 2021). In Appendix A, we consider extension to the more general case of arbitrary $\overline{\psi}_1$, $\overline{\psi}_2$. Due to the stagnation-free condition (11), the gradients of the streamfunction fluctuations are limited as

$$|\nabla\tilde{\psi}_i(\mathbf{x})| < |\nabla\overline{\psi}_i(\mathbf{x})|, \; i = 1, 2, \; \forall \mathbf{x} \in \Omega, \tag{20}$$

and so must be bounded. Similarly, we assume that the fluctuations $\tilde{\psi}_i(\mathbf{x})$ are also bounded. From Equations 13, 18 and 19 the mean and fluctuating components of the velocity field are

$$\overline{\mathbf{v}} = \overline{\psi}_1 \times \overline{\psi}_2 = \overline{v}\hat{\mathbf{e}}_1, \tilde{\mathbf{v}} = \nabla\tilde{\psi}_1 \times \nabla\tilde{\psi}_2 + \nabla\tilde{\psi}_1 \times \hat{\mathbf{e}}_3 - \nabla\tilde{\psi}_2 \times \overline{v}\hat{\mathbf{e}}_2. \tag{21}$$

We now show that the auxiliary variables χ_2, χ_3 that are associated with the transverse macrodispersion coefficients D^m_{22}, D^m_{33} may be expressed directly in terms of the streamfunction fluctuations as

$$\chi_2(\mathbf{x}) = -\frac{1}{\overline{v}}\tilde{\psi}_1(\mathbf{x}), \qquad \chi_3(\mathbf{x}) = -\tilde{\psi}_2(\mathbf{x}) \tag{22}$$

via substitution into Equation 7. For example, the LHS and RHS of Equation 7 for $j = 2$ ($\mathbf{v} \cdot \nabla\chi_2 = \tilde{v}_2$) are equivalent as

$$\begin{aligned}\mathbf{v}\cdot\nabla\chi_2 &= -\frac{1}{\overline{v}}\left(\overline{\mathbf{v}}+\tilde{\mathbf{v}}\right)\cdot\nabla\tilde{\psi}_1 = -\hat{\mathbf{e}}_1\cdot\nabla\tilde{\psi}_1 - (\hat{\mathbf{e}}_2\times\nabla\tilde{\psi}_2)\cdot\nabla\tilde{\psi}_1\\ &= \nabla\tilde{\psi}_1\cdot(\hat{\mathbf{e}}_3\times\hat{\mathbf{e}}_2) + \nabla\tilde{\psi}_1\cdot(\nabla\tilde{\psi}_2\times\hat{\mathbf{e}}_2)\\ &= \hat{\mathbf{e}}_2\cdot(\nabla\tilde{\psi}_1\times\nabla\tilde{\psi}_2) + \hat{\mathbf{e}}_2\cdot(\nabla\tilde{\psi}_1\times\hat{\mathbf{e}}_3)\\ &= \tilde{\mathbf{v}}\cdot\hat{\mathbf{e}}_2 = \tilde{v}_2,\end{aligned} \tag{23}$$

and likewise for $j=3$, $\mathbf{v}\cdot\nabla\chi_3 = \tilde{v}_3$. As the velocity deviation $\tilde{v}_2$ can be expressed as

$$\begin{aligned}\tilde{v}_2 &= \hat{\mathbf{e}}_2\cdot(\nabla\tilde{\psi}_1\times\nabla\tilde{\psi}_2) + \hat{\mathbf{e}}_2\cdot(\nabla\tilde{\psi}_1\times\hat{\mathbf{e}}_3)\\ &= \hat{\mathbf{e}}_2\cdot(\nabla\tilde{\psi}_1\times\nabla\tilde{\psi}_2) + \nabla\tilde{\psi}_1\cdot(\hat{\mathbf{e}}_3\times\hat{\mathbf{e}}_2)\\ &= \hat{\mathbf{e}}_2\cdot(\nabla\tilde{\psi}_1\times\nabla\tilde{\psi}_2) - \nabla\tilde{\psi}_1\cdot\hat{\mathbf{e}}_1,\end{aligned} \tag{24}$$

then substitution of $\tilde{v}_2$ and $\chi_2 = -\tilde{\psi}_1/\overline{v}$ into Equation 5 yields the following expression for the D^m_{22} transverse macrodispersion coefficient

$$D^m_{22} = \langle\tilde{v}_2\chi_2\rangle = \left\langle\frac{\tilde{\psi}_1}{\overline{v}}\hat{\mathbf{e}}_1\cdot\nabla\tilde{\psi}_1 - \frac{\tilde{\psi}_1}{\overline{v}}\hat{\mathbf{e}}_2\cdot(\nabla\tilde{\psi}_1\times\nabla\tilde{\psi}_2)\right\rangle, \tag{25}$$

and a similar expression can be obtained for D^m_{33}. From the vector identity $\nabla\cdot(\mathbf{a}\times\mathbf{b}) = (\nabla\times\mathbf{a})\cdot\mathbf{b} - (\nabla\times\mathbf{b})\cdot\mathbf{a}$, the expression

$$\frac{\tilde{\psi}_1}{\overline{v}}\hat{\mathbf{e}}_2\cdot(\nabla\tilde{\psi}_1\times\nabla\tilde{\psi}_2) = -\frac{\tilde{\psi}_1}{\overline{v}}\hat{\mathbf{e}}_2\cdot(\nabla\times\tilde{\psi}_2\nabla\tilde{\psi}_1) = \nabla\cdot\left(\tilde{\psi}_2\nabla\tilde{\psi}_1\times\frac{\tilde{\psi}_1}{\overline{v}}\hat{\mathbf{e}}_2\right),$$

hence (25) can be written as

$$\begin{aligned}D^m_{22} &= \left\langle\frac{\tilde{\psi}_1}{\overline{v}}\hat{\mathbf{e}}_1\cdot\nabla\tilde{\psi}_1 - \nabla\cdot\left(\frac{\tilde{\psi}_1\tilde{\psi}_2}{\overline{v}}\nabla\tilde{\psi}_1\times\hat{\mathbf{e}}_2\right)\right\rangle\\ &= \left\langle\nabla\cdot\left(\frac{\tilde{\psi}_1^2}{2\overline{v}}\hat{\mathbf{e}}_1 - \frac{\tilde{\psi}_1\tilde{\psi}_2}{\overline{v}}\nabla\tilde{\psi}_1\times\hat{\mathbf{e}}_2\right)\right\rangle \equiv \langle\nabla\cdot\mathbf{f}(\mathbf{x})\rangle,\end{aligned} \tag{26}$$

and substitution into Equation 3 yields

$$D^m_{22} = \lim_{V\to\infty}\frac{1}{V}\int_V\nabla\cdot\mathbf{f}(\mathbf{x})d^3\mathbf{x} = \lim_{V\to\infty}\frac{1}{V}\oint_{\partial V}\mathbf{n}\cdot\mathbf{f}(\mathbf{x})d^2\mathbf{x}. \tag{27}$$

As the values of $\mathbf{f}(\mathbf{x})$ in Equation 26 are finite in the limit $|\mathbf{x}|\to\infty$, then if the volume V is represented as a cube of length L, the surface integral in Equation 27 scales as L^2, whereas $1/V$ scales as $1/L^3$, hence $D^m_{22}\to 0$ as $V\to\infty$ and $L\to\infty$. Similar arguments show that D^m_{33} is also zero. These results can be extended to the general case $\overline{\mathbf{v}} = \overline{v}\hat{\mathbf{e}}_1$, where the mean field components of the streamfunctions are

$$\overline{\psi}_1(\mathbf{x}) = a_1x_2 + b_1x_3, \overline{\psi}_2(\mathbf{x}) = a_2x_2 + b_2x_3, \tag{28}$$

where $\overline{v}\equiv a_1b_2 - a_2b_1\neq 0$. In this case the auxillary variables χ_2, χ_3 are given in terms of the streamfunction fluctuations as

$$\chi_2(\mathbf{x}) = \frac{1}{\overline{v}}(b_1\tilde{\psi}_2(\mathbf{x}) - b_2\tilde{\psi}_1(\mathbf{x})), \tag{29}$$

$$\chi_3(\mathbf{x}) = \frac{1}{\overline{v}}(a_2\tilde{\psi}_1(\mathbf{x}) - a_1\tilde{\psi}_2(\mathbf{x})). \tag{30}$$

In Appendix A we show that these auxillary variables satisfy (7) and also yield the result that the transverse macrodispersion coefficients D^m_{22}, D^m_{33} are both zero. Therefore, the existence of the streamfunctions ψ_1, ψ_2 in steady isotropic 3D Darcy flow forbids the presence of transverse macrodispersion in the limit of vanishing local dispersion.

Table 1
Numerical Solver and Multi-Gaussian Log-Conductivity Field Parameters for

Parameter	Value
Domain Ω	$\mathbb{T}^3 = [0,1] \times [0,1] \times [0,1]$
Log-conductivity mean $\langle \ln k \rangle$	1
Log-conductivity variance $\sigma^2_{\ln k}$	4
Correlation length ℓ	1/16
Grid resolution Δ_0	1/256
Grid points per correlation length ℓ/Δ_0	16
Mean velocity v	1
Finite difference residual	10^{-16}

5. Numerical Computation of Transverse Macrodispersion

5.1. Streamfunctions and Conductivity Fields

In this section we examine the ability of conventional numerical particle tracking schemes to enforce the kinematic constraints associated with isotropic Darcy flow and the associated impacts upon computational of transverse macrodispersion. We also present a novel particle tracking method that explicitly enforces these kinematic constraints. Particle tracking comprises of two distinct steps, either of which can lead to violation of these kinematic constraints. First, naive interpolation of the velocity field from discrete data (whether as a post-processing step for mesh-based numerical schemes or implicit in mesh-less flow solvers) may violate the helicity-free constraint associated with isotropic Darcy flow. Second, even if the velocity field is helicity-free, an integration scheme must be employed that ensures computed streamlines adhere to these kinematic constraints and associated invariants - in the case of isotropic Darcy flow, this corresponds to streamfunctions remaining constant along computed streamlines. Hence the kinematic constraints are adhered to only when both the velocity field reconstruction and streamline computation methods satisfy the above requirements.

To investigate the ability of conventional velocity reconstruction and streamline integration methods to enforce these constraints and the impacts upon macrodispersion, we consider numerical particle tracking in a heterogeneous and smooth isotropic Darcy flow. Following the proof in Section 4, this class of flow exhibits zero transverse macrodispersion, hence the transverse macrodispersion computed by these methods is entirely spurious. We consider this zero helicity density flow in the triply-periodic unit cube (3-torus) Ω: $\mathbf{x} \in [0,1] \times [0,1] \times [0,1]$ with Born-von Kármán boundary conditions, which allows simulation of flow and transport in an unbounded domain via periodic translation of the base flow $\mathbf{v}(\mathbf{x})$ in Ω as

$$\mathbf{v}_\infty(\mathbf{x}) = \mathbf{v}(x_1 \mathrm{mod} 1, x_2 \mathrm{mod} 1, x_3 \mathrm{mod} 1). \tag{31}$$

We note that periodicity of this flow does not necessarily enforce zero transverse dispersion. Indeed it is well known that steady periodic 3D flows that admit chaotic advection posses aperiodic streamlines that may wander throughout the flow domain, leading to finite transverse macrodispersion. Conversely, integrable steady 3D periodic flows (such as zero helicity flows) admit periodic streamlines and hence zero transverse macrodispersion. The zero helicity density fluid velocity field $\mathbf{v}(\mathbf{x})$ is represented in terms of the dual streamfunctions $\psi_1(\mathbf{x})$, $\psi_2(\mathbf{x})$ of the flow, which are computed to high precision for a heterogeneous porous medium with a locally isotropic hydraulic conductivity field $k(\mathbf{x})$ that is described by a log-Gaussian isotropic random field with correlation length $\ell = 1/16$, log-mean $\langle \ln k \rangle = 1$ and log-variance $\sigma^2_{\ln k} = 4$, as summarized in Table 1. Lester et al. (2021) show that numerical solution of the governing Equation (14) for these streamfunctions converge to the same velocity field $\mathbf{v}(\mathbf{x})$ as that given numerical solution of the isotropic Darcy Equation 9. The streamfunctions are decomposed into fluctuating components $\tilde{\psi}_1(\mathbf{x})$, $\tilde{\psi}_2(\mathbf{x})$ and mean field components $\overline{\psi}_1 = x_2$, $\overline{\psi}_2 = x_3$, such that the mean velocity $\overline{\mathbf{v}} = \nabla\overline{\psi}_1 \times \nabla\overline{\psi}_2 = v\hat{\mathbf{e}}_1$ ad $v = 1$. The unknown fluctuating components $\tilde{\psi}_1$, $\tilde{\psi}_2$ are determined via finite difference solution of Equation 14 subject to periodic boundary conditions. Due to the coupled nonlinear source terms S_1, S_2, the finite difference equations are solved by first solving the homogenized governing Equation 14 with $S_1 = S_2 = 0$ via an iterative Krylov sparse method to provide an initial estimate of $\tilde{\psi}_1(\mathbf{x})$, $\tilde{\psi}_2(\mathbf{x})$ on a 256^3 regular grid (with spacing $\Delta_0 = 1/256$) over the flow domain. This discretization corresponds to a mesh resolution of $\ell/\Delta_0 = 16$ grid points per correlation length. Next, an explicit time-stepping method with variable time-step is used to solve the full inhomogeneous Equation 14 to precision 10^{-16}. Periodic cubic splines are used to interpolate the grid-based values of ψ_1 and ψ_2 to generate continuous analytic expressions for $\psi_1(\mathbf{x})$, $\psi_2(\mathbf{x})$ throughout the flow domain, and typical streamsurfaces are shown in Figure 1a. Although the fields $\psi_1(\mathbf{x})$, $\psi_2(\mathbf{x})$ contain small numerical errors associated with spatial discretization and interpolation, for the purpose of testing particle tracking methods we treat these interpolated streamfunctions as being exact, which facilitates direct comparison of computed particle trajectories with the streamlines formed by $\psi_1(\mathbf{x})$, $\psi_2(\mathbf{x})$. As shown in Figure 2b, the resultant velocity field generated from these interpolated streamfunctions is not exactly helicity-free (although it is exactly divergence-free from Equation 13). This however does not violate the kinematic constraints associated

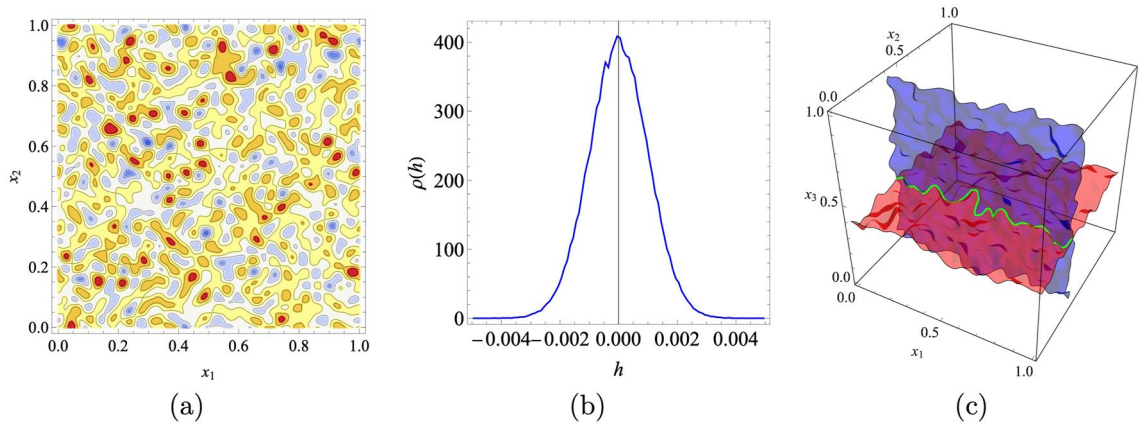

Figure 2. (a) 2D cross section of the 3D log-conductivity field ln $k(\mathbf{x})$ at $x_3 = 0.5$. (b) Distribution of helicity density values h from numerically interpolated streamfunctions ψ_1, ψ_2. (c) Typical streamsurfaces ψ_1 (blue), ψ_2 (red) and corresponding streamline (green) for isotropic Darcy flow.

with isotropic Darcy flow, as these constraints arise from the existence of a pair of streamfunctions and the helicity-free condition is a necessary but not sufficient condition for the existence of streamfunctions.

5.2. Velocity Reconstruction Errors

To demonstrate how the errors associated with velocity reconstruction methods can generate spurious transverse macrodispersion in steady 3D flow, we consider the Pollock algorithm (Pollock, 1988) as an example that is used in many groundwater transport codes. It is important to note that while many conventional particle tracking methods produce particle trajectories that do not exactly follow streamlines in steady 2D flows, the trajectories computed by these methods are still confined to the 2D domain and do not cross (as the methods are numerically consistent and stable), and so cannot diverge without bound, leading to zero asymptotic transverse macrodispersion in the purely advective limit. Conversely, for 3D flows that admit pairs of 2D streamsurfaces, particle trajectories can wander off these streamsurfaces due to numerical errors, leading to spurious transverse macrodispersion.

The Pollock algorithm is based upon linear interpolation of grid-based fluid velocity data at cell faces, leading to an approximation of the velocity field in a zero-order Raviart-Thomas-Nédélec function space on cuboid elements (Nédélec, 1980; Raviart & Thomas., 1977). Although this representation can ensure the divergence-free condition of the velocity field is enforced, it cannot also ensure the curl and hence helicity is correctly captured (Nédélec, 1980; Raviart & Thomas., 1977).

Unless the helicity-free condition is explicitly imposed, such interpolation inevitably leads to an interior velocity field that is not exactly helicity-free. Furthermore, the helicity-free condition is violated over cell faces as the velocity gradient here is discontinuous. Hence the associated streamlines do not adhere to the kinematic constraints of these flows, regardless of the specific integration routine. Although higher-order interpolation schemes such as divergence-free cubic interpolation (Ravu et al., 2016) can generate smooth and more accurate reconstructed velocity fields, they still do not explicitly impose the helicity-free condition.

One kinematically-consistent velocity reconstruction method is to employ an interpolation scheme that is inherently helicity-free, via interpolation of gridded potential and conductivity datasets to yield smooth and continuous potential $\phi(\mathbf{x})$ and scalar conductivity $k(\mathbf{x})$ fields. Representation of the velocity field via (9), (where the divergence of $\phi(\mathbf{x})$ is performed analytically) ensures the velocity field is helicity-free (Lester et al., 2019), even if the potential field contains small numerical errors and the resultant velocity is not strictly divergence-free. Another approach is to solve the streamfunctions ψ_1, ψ_2, and perform interpolation on the gridded streamfunction datasets under the constraints $\nabla\psi_1(\mathbf{x}) \neq \mathbf{0}$, $\nabla\psi_2(\mathbf{x}) \neq \mathbf{0}$. These constraints ensure the Lagrangian kinematics of the flow are identical to a helicity-free flow, and the associated velocity field is also exactly divergence free.

In this example we focus on the Pollock particle tracking algorithm as it is exact, hence all of the errors reported here stem solely from the linear velocity reconstruction method. While in standard groundwater-flow codes

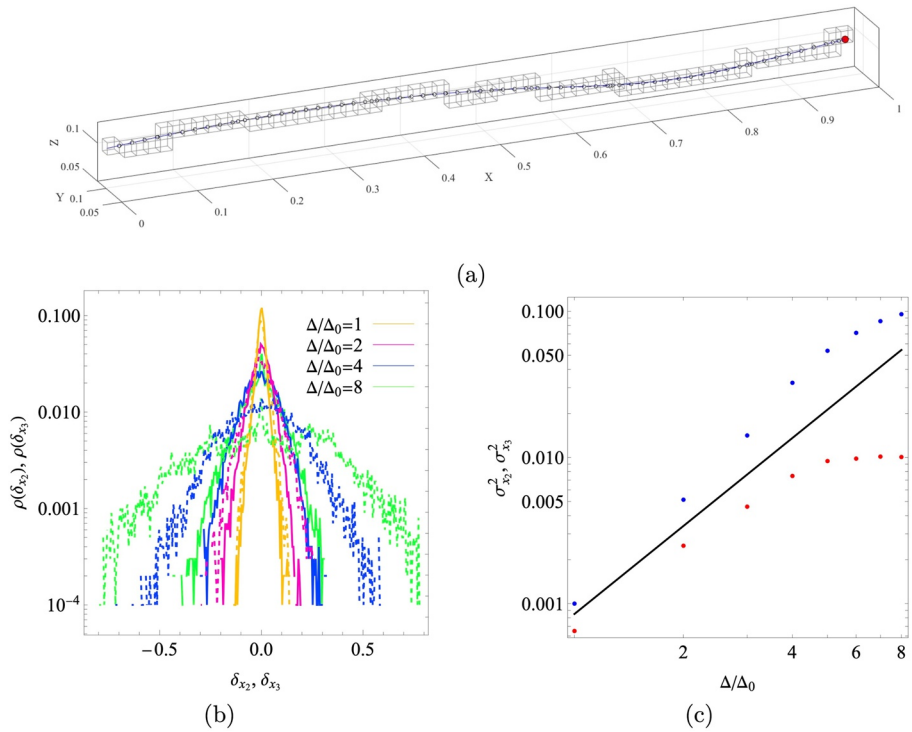

Figure 3. (a) Typical trajectory and associated grid cells used for computation for a single particle through the domain Ω under the Pollock algorithm. (b) PDFs of the spatial errors δ_{x_2} (dashed), δ_{x_3} (solid) for different levels of the spatial discretization Δ/Δ_0, (c) Growth of the variance $\sigma^2_{x_2}$ (blue dots), $\sigma^2_{x_3}$ (red dots) of the spatial errors δ_{x_2}, δ_{x_3} for different levels of the spatial discretization Δ/Δ_0. These variances grow roughly as $(\Delta/\Delta_0)^2$, as indicated by the solid black line.

using Pollock's method the velocity field arises from the cell-centered Finite Volume discretization of the groundwater-flow equation using cuboidal cells, in this study the cell face velocities v^i are computed directly from the streamfunctions over the 256^3 finite difference grid via Stokes theorem as

$$\begin{aligned} v_i^{pqr} &= \frac{1}{\Delta_0^2}\int_{x_{j,pq}}^{x_{j,pq}+\Delta_0}\int_{x_{k,qr}}^{x_{k,pq}+\Delta_0}(\nabla\psi_1(\mathbf{x})\times\nabla\psi_2(\mathbf{x}))\cdot\hat{\mathbf{e}}_i dx_j dx_k \\ &= \frac{1}{\Delta_0^2}\iint_{S_i^{pqr}}(\nabla\times\psi_1(\mathbf{x})\nabla\psi_2(\mathbf{x}))\cdot\hat{\mathbf{e}}_i d^d x \\ &= \frac{1}{\Delta_0^2}\oint_{\partial S_i^{pqr}}\psi_1(\mathbf{x})\nabla\psi_2(\mathbf{x})\cdot\mathbf{n}dx, \quad i=1:3, \end{aligned} \tag{32}$$

where S_i^{pqr} denotes the grid cell face oriented in the i-direction and located at the grid coordinates (p, q, r) and ∂S_i^{pqr} denotes the boundary of this face, and $\mathbf{n}$ is the unit vector oriented along the boundary of S_i^{pqr}. The inherently divergence free nature of the dual streamfunction representation (13) ensures that the cell face velocities are also divergence-free in discretized form over a grid cell, that is,

$$v_1^{pqr} - v_1^{p-1qr} + v_2^{pqr} - v_2^{pq-1r} + v_3^{pqr} - v_3^{pqr-1} = 0. \tag{33}$$

Hence the computed face velocities used in the Pollock algorithm are divergence-free to machine precision. We also consider performance of the Pollock algorithm on coarser grids with spacing $\Delta/\Delta_0 = 1, 2\ldots, 8$ by appropriately averaging over the cell face velocities in Equation 33.

The Pollock algorithm is based upon linear interpolation of the cell face velocities v_i^{pqr} (or their coarse-grained counterparts) to compute the velocity field within each grid cell. Note that the velocity gradient is discontinuous at each cell interface as the interpolated velocity is piecewise linear. Given an arbitrary particle position on any face of any grid cell, the particle trajectory and travel time is computed analytically from this linear velocity field. The exit position of a particle from the current cell then forms the entry position for the new cell, and this computational procedure continues from cell to cell to traverse the flow domain. Figure 3a shows a typical particle trajectory

and associated grid cells for the Pollock algorithm in the 3D domain Ω for the steady 3D isotropic Darcy flow described above. As the Pollock algorithm uses linear interpolation of the velocity field within each grid cell and analytic solutions for the particle trajectory within each cell, the only control parameter for this method is the cell size Δ. The linear nature of the interpolated velocity field means that the error of the Pollock algorithm is second order in space, and so the spatial error of the numerically computed particle trajectories is expected to scale as Δ^2.

As streamlines are periodic within Ω (due to periodicity of the streamfunctions), the error between the computed i-th particle trajectory over Ω and the exact streamline can be expressed in terms of the spatial errors in the x_2 and x_3 directions as

$$\delta_{x_2,i} = x_{2,1,i} - x_{2,0,i}\ \delta_{x_3,i} = x_{3,1,i} - x_{3,0,i}, \tag{34}$$

and the corresponding streamfunction errors are

$$e_{\psi_1,i} = \psi_1(\mathbf{x}_{1,i}) - \psi_1(\mathbf{x}_{0,i})\ e_{\psi_2,i} = \psi_2(\mathbf{x}_{1,i}) - \psi_2(\mathbf{x}_{0,i}). \tag{35}$$

As shown in Figure 3b, the spatial errors $\delta_{x_2,i}$, $\delta_{x_3,i}$ over Ω are normally distributed with zero mean and finite variance $\sigma^2_{x_2}$, $\sigma^2_{x_3}$. Figure 3c shows that, as expected, these errors variances increase with square of the spatial discretization, $\sigma^2_{x_i} \sim (\Delta/\Delta_0)^2$, $i = 1, 2$ as the Pollock method is second order in space. These errors characterize the failure of the Pollock algorithm to follow the analytic streamline, which arises from the linear interpolation of the grid cell velocity from the discrete face values. From Figure 3, the variance of the x_3 errors is significantly larger than that of the x_2 errors. As expected, the streamfunction errors $e_{\psi_1,i}$, $e_{\psi_2,i}$ are strongly correlated with the spatial errors, and so are not shown. Under the assumption that the variances $\sigma^2_{x_i}$ grow linearly with time, then the Pollock algorithm predicts the transverse macrodispersion coefficients

$$D^m_{22} = \frac{1}{2\langle\tau_\Omega\rangle}\sigma^2_{x_2}\ D^m_{33} = \frac{1}{2\langle\tau_\Omega\rangle}\sigma^2_{x_3}, \tag{36}$$

where $\langle\tau_\Omega\rangle$ is the mean residence time of all streamlines over the domain Ω. Hence, care must be taken when analyzing results from the Pollock algorithm as there is potential to misinterpret these spatial errors as transverse macrodispersion. One approach is to remedy this is to perform rigorous convergence studies with respect to the grid size Δ to ensure results are mesh-independent, however Figure 3 indicates that even highly resolved grids (such as Δ_0 that uses 16 grid points per correlation length) can impart significant spatial errors.

5.3. Streamline Integration Errors

To analyze the numerical errors associated with conventional streamline integration methods, we use a 4th order Runge-Kutta algorithm with an adaptive step size to achieve a prescribed tolerance tol for the particle tracking. In this case the velocity field passed to the Runge-Kutta algorithm is exact (i.e., is given in terms of the interpolated streamfunctions $\psi_1(\mathbf{x})$, $\psi_2(\mathbf{x})$), and so the particle tracking errors in this case stem solely from the streamline integration tolerance, tol, which is tested over the range 10^{-4}-10^{-8}. Figure 4a shows that the spatial errors δ_{x_2}, δ_{x_3} for the Runge-Kutta algorithm also have zero mean and finite variance over the range of tolerances tested. As shown in Figure 4b, the spatial errors associated with the Runge-Kutta algorithm are of significantly smaller magnitude than the Pollock algorithm, and the variances $\sigma^2_{x_2}$, $\sigma^2_{x_3}$, grow as $\sqrt{\text{tol}}$.

Thus, the spatial errors associated with the Runge-Kutta method also have the potential to be interpreted as transverse macrodispersion, and the transverse dispersivities are also given by Equation 36. This dispersion decays to zero as the tolerance tol limits toward zero, again highlighting the need for rigorous convergence studies to determine the true dispersion coefficients D^m_{22}, D^m_{33}. This behavior is expected to persist for all streamline integration methods that do no explicitly preserve the streamfunctions of isotropic Darcy flow, leading to the potential for spurious predictions of finite transverse macrodispersion.

5.4. Pseudo-Symplectic Particle Tracking Algorithm

An alternative particle tracking method that does not induce spurious transverse macrodispersion is given by 1D integration along streamlines (similar to Equation 17), rather then numerical solution of the 3D advection ODE (16). This method addresses the issues related to velocity reconstruction and streamline integration, and shares

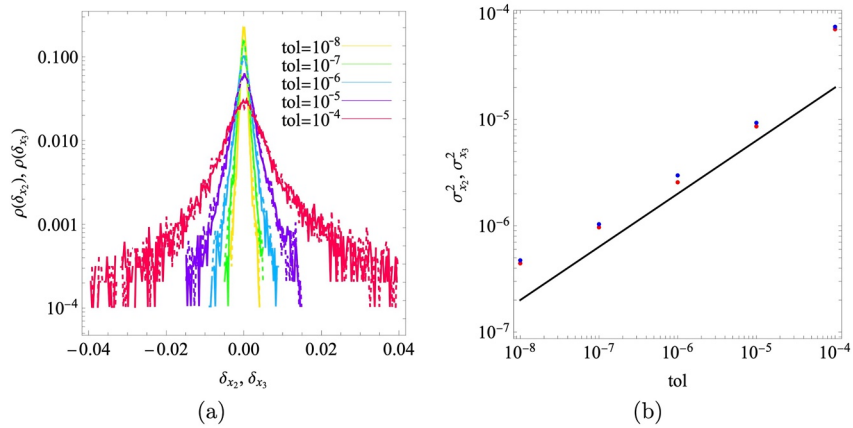

Figure 4. (a) PDFs of the spatial errors δ_{x_2}, δ_{x_3} for the Runge-Kutta algorithm for different values of the tolerance tol. (b) Growth of the variance $\sigma^2_{x_2}$ (solid), $\sigma^2_{x_3}$ (dashed) of the spatial errors δ_{x_2}, δ_{x_3} for different tolerances. These variances grow roughly as $\sqrt{\text{tol}}$, as indicated by the solid black line.

characteristics with symplectic integration methods for Hamiltonian systems (Sanz-Serna, 1992), whereby the Hamiltonian is explicitly conserved by the integration routine. For steady 2D flows, the advection equation is Hamiltonian where the 2D streamfunction is the system Hamiltonian and (x_1, x_2) form the canonical coordinates of the system and the streamfunction is conserved along particle trajectories. For helicity-free steady 3D flows, the advection Equation 16 is not Hamiltonian as the degrees of freedom (3) of the system are odd. Hence the dual streamfunctions ψ_1, ψ_2 are not Hamiltonians, but they are invariants that are conserved along particle trajectories (streamlines) that are solutions to the advection Equation 16. Thus we seek to develop a *pseudo-symplectic* particle tracking method that explicitly conserves the invariants ψ_1, ψ_2.

It is important to note that even if the numerically computed streamfunctions ψ_1, ψ_2 (including their interpolants) contain numerical errors, the existence of a pair of streamfunctions (given satisfaction of the stagnation-free condition (11)) is sufficient to ensure that the kinematic constraints of helicity-free flows are satisfied. Thus, the integration routine must also ensure these streamfunctions are preserved along streamlines. This is achieved by first computing the streamfunctions $\psi_1(\mathbf{x})$, $\psi_2(\mathbf{x})$ via Equation 14, and then determining the inverse functions

$$x_2 = X_2(\psi_1, \psi_2, x_1), \quad x_3 = X_3(\psi_1, \psi_2, x_1), \tag{37}$$

which are unique due to the stagnation-free conditions $\nabla\psi_1(\mathbf{x}) \neq \mathbf{0}$, $\nabla\psi_2(\mathbf{x}) \neq \mathbf{0}$. The inverse functions X_2, X_3 may be approximated numerically by using the values of ψ_1, ψ_2 on the 3D finite difference grid used to solve (14). The structured finite difference grid in (x_1, x_2, x_3) space is then projected onto the corresponding unstructured grid in (x_1, ψ_1, ψ_2) space, and then interpolation is performed over this unstructured grid to yield $X_2(\psi_1, \psi_2, x_1)$, $X_3(\psi_1, \psi_2, x_1)$. Hence the error associated with these inverse functions arises from the interpolation process. Using these inverse functions, the x_1 component of the velocity field $\mathbf{v}(\mathbf{x})$ can then be expressed as $v_1(x_1, x_2, x_3) = v_1(x_1, X_2(\psi_1, \psi_2, x_1), X_3(\psi_1, \psi_2, x_1))$, and the x_1 component of the advection Equation 16 simplifies to the 1D integral

$$\frac{dx_1}{dt} = v_1(x_1, x_2, x_3) \Rightarrow t(x_1) = \int_0^t \frac{dx_1}{v_1(x_1, X_2(\psi_{1,0}, \psi_{2,0}, x_1), X_3(\psi_{1,0}, \psi_{2,0}, x_1))}, \tag{38}$$

where the invariant streamfunction values $\psi_{1,0} = \psi_1(\mathbf{x}_0)$, $\psi_{2,0} = \psi_2(\mathbf{x}_0)$ are given by the particle initial position $\mathbf{x}_0$. This simplification of the advection ODE (16) to the integral (38) not only simplifies numerical particle tracking, but it also ensures that the kinematic constraints associated with helicity-free flows are explicitly conserved.

A wide range of high-precision numerical techniques can be used to perform the integration (38), and these determine the accuracy of the advection time t, but do not impact the accuracy of the particle trajectory due to the form of Equation 38. Conversely, spatial particle tracking errors arise from the interpolation routine used to determine the inverse functions X_2, X_3. However, even if these interpolation errors are significant, the transverse macrodispersion coefficients D^m_{22}, D^m_{33} computed by this algorithm are still zero because the streamfunction formulation in Equation 38 still enforces the kinematic constraints inherent to steady 3D isotropic Darcy flow. Hence

computation of the streamfunctions $\psi_1(\mathbf{x})$, $\psi_2(\mathbf{x})$ via Equation 14 provide a means to numerically study transport and dispersion in isotropic Darcy flow while explicitly preserving the inherent topological structure of these flows. We do not implement this algorithm to transverse dispersion in the purely advective case as the results are trivial (i.e., $\delta_{x_2} = \delta_{x_3} = 0, \Rightarrow D^m_{22} = D^m_{33} = 0$), but it is employed in the following section to study the impact of local dispersion. This pseudo-symplectic method demonstrates the utility of the streamfunction representation (13) for helicity-free flows and the importance of explicitly preserving their inherent kinematic constraints.

6. Impact of Local Dispersion

6.1. Theoretical Analysis

The pseudo-symplectic method developed in Section 5.4 can be used to determine the impact of local dispersion upon transverse macrodispersion while ensuring the purely advective particle trajectories satisfy the kinematic constraints of locally isotropic Darcy flow. We consider the case of molecular diffusion, where $\mathbf{D}_0 = D_0\mathbf{I}$ and D_0 is the molecular diffusivity, and so the Pèclet number is then $Pe = \overline{v}\ell/D_0$. Under these conditions, the position $\mathbf{x}_p(t)$ of a diffusive solute molecule with initial position $\mathbf{x}_0$ follows the stochastic Langevin equation

$$\begin{aligned}\frac{d\mathbf{x}_p}{dt} &= \mathbf{v}(\mathbf{x}_p(t)) + \sqrt{2D_0}\boldsymbol{\xi}(t), \quad \mathbf{x}_p(0) = \mathbf{x}_0,\\ &= \sqrt{2D_0}\boldsymbol{\xi}(t) + \mathbf{v}\left(\mathbf{x}^0(t)\right) + \left[\mathbf{x}_p(t) - \mathbf{x}^0(t)\right]\cdot\nabla\mathbf{v}\left(\mathbf{x}^0(t)\right) + \text{h.o.t.},\end{aligned} \tag{39}$$

where $\boldsymbol{\xi}(t)$ is a delta-correlated Gaussian white noise with zero mean and covariance $\langle\xi_i(t)\xi_j(t')\rangle = \delta_{ij}\delta(t-t')$, δ_{ij} is the Knoecker delta and $\delta(t)$ is the Dirac delta. Here, $\mathbf{x}^0(t)$ is the trajectory of a non-diffusive tracer particle with initial position $\mathbf{x}^0(0) = \mathbf{x}_0$ and h.o.t. refers to higher order terms in the Taylor series expansion in Equation 39. In the limit of large Pe, the Langevin Equation 39 over the periodic domain Ω may be approximated as

$$\frac{d\mathbf{x}_p}{dt} \approx \mathbf{v}\left(\mathbf{x}^0(t)\right) + \sqrt{2D_0}\boldsymbol{\xi}(t). \tag{40}$$

As terms of the order $\nabla\mathbf{v}$ and higher are ignored in Equation 40, this approximation ignores the impact of fluid deformation history upon the diffusion process. Due to periodicity of the streamlines in Ω, under this approximation the position of the solute molecule along a streamline with advection time τ_Ω through Ω is then

$$\mathbf{x}_p(t+\tau_\Omega) = \mathbf{x}_p(t) + \hat{\mathbf{e}}_1 + \sqrt{2D_0\tau_\Omega}\boldsymbol{\xi}, \quad \mathbf{x}_p(0) = \mathbf{x}_0, \tag{41}$$

where $\boldsymbol{\xi}$ is a Gaussian variable with zero mean and variance $\langle\xi_i\xi_j\rangle = \delta_{ij}$. In the limit $Pe \gg 1$ we may ignore diffusion in the axial direction, and so under the random re-injection protocol the transverse displacements $\Delta_i \equiv x_{p,i} - x^0_i$ between the solute molecule and the streamline evolves via the continuous time random walk (CTRW)

$$\Delta_{2,n+1} = \Delta_{2,n} + \sqrt{2D_0\tau_{\Omega,n}}\xi_2 \; \Delta_{3,n+1} = \Delta_{3,n} + \sqrt{2D_0\tau_{\Omega,n}}\xi_3, \tag{42}$$

where $\Delta_{i,n}$ is the displacement in the i-coordinate at axial distance $x_1 = ln$. Thus the variance of the local displacements evolve with n and t as $\sigma^2_{i,n}(t) = 2D_0\langle\tau_\Omega\rangle n = 2D_0 t$, $i = 2, 3$, and so the asymptotic transverse macrodispersion coefficients are both zero as

$$D_0 + D^m_{ii} = \frac{1}{2}\lim_{t\to\infty}\frac{d}{dt}\sigma^2_{i,n}(t) = D_0 \quad \Rightarrow \quad D^m_{22} = 0, \quad D^m_{33} = 0. \tag{43}$$

This result is to be expected in locally isotropic Darcy flow when fluid deformation is ignored as the transverse distance between streamlines can only fluctuate with longitudinal distance. In this case, local dispersion is the only mechanism to generate persistent macrodispersion as neighboring streamlines cannot continually diverge due to the kinematic constraints of these flows.

The impact of fluid deformation upon transverse dispersion can be quantified to leading order in terms of the deformation gradient tensor $\mathbf{F}(t)$ that evolves along the streamline $\mathbf{x}^0(t)$ as

$$\frac{d\mathbf{F}(t)}{dt} = \left[\nabla\mathbf{v}\left(\mathbf{x}^0(t)\right)\right]^\top\cdot\mathbf{F}(t), \quad \mathbf{F}(0) = \mathbf{I}, \tag{44}$$

where $\mathbf{I}$ is the identity matrix. This corresponds to truncation of Equation 39 to first order in space (i.e., by neglecting h.o.t.), which also corresponds to a solute plume which has a Gaussian profile in space. Although the

truncation of Equation 39 to first order is a restrictive assumption (as most plumes in heterogeneous media are non-Gaussian), such truncation still provides insights into the interactions between the Lagrangian kinematics and local dispersion.

For an evolving 3D Gaussian solute blob with initial position $\mathbf{x}_0$, maximum concentration $c_{m,0}$ and covariance matrix $\mathbf{\Sigma}_0$, the spatial concentration field in a d-dimensional flow field is given as

$$c(\mathbf{x},t)=\frac{c_{m,0}}{\sqrt{(2\pi)^d \det \mathbf{\Sigma}(t)}}\exp\Big(-\frac{1}{2}\big(\mathbf{x}-\mathbf{x}^0(t)\big)^{\top}\cdot\mathbf{\Sigma}^{-1}(t)\cdot\big(\mathbf{x}-\mathbf{x}^0(t)\big)\Big), \tag{45}$$

where the covariance matrix $\mathbf{\Sigma}(t)\equiv\mathbf{\Delta}(t)+2D_0\mathbf{\Lambda}(t)$. Here $\mathbf{\Delta}(t)$ encodes deformation of the initial blob due to fluid deformation

$$\mathbf{\Delta}(t)=\mathbf{F}^{-1}(t)\cdot\mathbf{\Sigma}_0\cdot\mathbf{F}^{-\top}(t), \tag{46}$$

and $\mathbf{\Lambda}(t)$ represents variance growth of the blob due to augmented diffusion via the deformation history along the fluid trajectory $\mathbf{x}_0(t)$:

$$\mathbf{\Lambda}(t)\equiv\int_0^t\mathbf{F}^{-1}\big(t'\big)\cdot\mathbf{F}^{-\top}\big(t'\big)dt'. \tag{47}$$

Lester et al. (2022) show that for isotropic Darcy flow the deformation tensor $\mathbf{F}'(t)$ is upper triangular in a coordinate frame $\mathbf{x}'$ aligned with the flow direction x_1' and the two streamfunction directions x_2', x_3'. The diagonal components of $\mathbf{F}'(t)$ are given as

$$F'_{11}(t)=\frac{v(t)}{v(0)}\qquad F'_{22}(t)=\sqrt{\frac{v(0)m(t)}{v(t)m(0)}}\qquad F'_{33}(t)=\sqrt{\frac{v(0)m(0)}{v(t)m(t)}}, \tag{48}$$

where $m\equiv|\nabla\psi_2|/|\nabla\psi_1|$ characterizes the relative gradients of the streamfunctions, and for statistically stationary and isotropic porous media, the PDF of $\ln m$ is symmetric about $\ln m=0$. From Equation 47, the (2, 3) components of $\mathbf{\Lambda}(t)$ that are transverse to the streamlines are given by the submatrix $\mathbf{\Lambda}_\perp(t)$ then evolve as

$$\mathbf{\Lambda}_\perp(t)=\int_0^t\begin{pmatrix}\frac{1}{F'^2_{22}(t')} & 0\\ 0 & \frac{1}{F'^2_{33}(t')}\end{pmatrix}dt'. \tag{49}$$

Le Borgne et al. (2008) and Lester et al. (2022) respectively show that for 2D and 3D heterogeneous Darcy flow, the velocity magnitude v and streamfunction gradient ratio m both undergo Markovian spatial decorrelation along streamlines (with the same decorrelation length ℓ), and so the random components v and m may be described by a CTRW in terms of the distance s along each streamline. As such, we recast the integral (49) in terms of the streamline distance s via the transform $v=ds/dt$, yielding

$$\mathbf{\Lambda}_\perp(s)=\frac{1}{v(0)}\int_0^s\begin{pmatrix}\frac{m(0)}{m(s')} & 0\\ 0 & \frac{m(s')}{m(0)}\end{pmatrix}ds', \tag{50}$$

and so the PDFs of the diagonal components of $\mathbf{\Lambda}_\perp$ are given by

$$\Lambda_{\perp,22}(s)\approx\frac{\ell m(0)}{v(0)}\sum_{n=1}^{N_s}\frac{1}{m_n},\quad \Lambda_{\perp,33}(s)\approx\frac{\ell}{v(0)m(0)}\sum_{n=1}^{N_s}m_n, \tag{51}$$

where $N_s=\lfloor s/\ell\rfloor$. The rescaled components $L_{22}\equiv\Lambda_{\perp,22}v(0)/(\ell m(0))$, $L_{33}\equiv\Lambda_{\perp,33}v(0)m(0)/\ell$ follow the CTRW

$$L_{22,n+1}=L_{22,n}+\frac{1}{m_n}\qquad L_{33,n+1}=L_{33,n}+m_n\qquad t_{n+1}=t_n+\tau_n, \tag{52}$$

where the subscript n denotes the variable at $s=\ell n$, and the waiting time $\tau_n=\ell/v_n$. For many flows in heterogeneous porous media, the PDF ρ_v of the Eulerian velocity magnitude v scales as a power-law in the low-velocity limit with index $\beta>1$,

$$\rho_v(v) \sim v^{\beta-1}, \quad \text{for } v \ll \langle v \rangle, \tag{53}$$

which corresponds to power-law decay of the transition time distribution $\psi(\tau)$ at long times as

$$\psi(\tau) \sim \tau^{-\beta-1}, \quad \text{for } \tau \gg \langle \tau \rangle. \tag{54}$$

For $\beta > 1$ the mean waiting time based on the flux-weighted velocity $\langle \tau \rangle = \ell/\langle v \rangle$ is well defined, and so in the asymptotic limit $n \to \infty$, $t_n \to n\ell\langle 1/v \rangle$, $L_{22,n} \to n\langle 1/\mathrm{m} \rangle$ and $L_{33,n} \to n\langle m \rangle$. Hence the averages of $L_{22}(t)$, $L_{33}(t)$ along a streamline evolve as

$$\langle L_{22}(t) \rangle = \langle v \rangle \left\langle \frac{1}{m} \right\rangle \frac{t}{\ell}, \quad \langle L_{33}(t) \rangle = \langle v \rangle \langle m \rangle \frac{t}{\ell}, \tag{55}$$

and the ensemble averages of $\Lambda_\perp(t)$ grow at a constant rate in the asymptotic limit as

$$\lim_{t\to\infty} \frac{d}{dt} \langle \Lambda_{\perp,22}(t) \rangle = \left\langle \frac{m(0)}{v(0)} \right\rangle \langle v \rangle \left\langle \frac{1}{m} \right\rangle, \tag{56}$$

$$\lim_{t\to\infty} \frac{d}{dt} \langle \Lambda_{\perp,33}(t) \rangle = \left\langle \frac{1}{v(0)m(0)} \right\rangle \langle v \rangle \langle m \rangle. \tag{57}$$

For Gaussian-shaped solute injection with initial covariance matrix $\mathbf{\Sigma}_0$ and position $\mathbf{x}_0$, the ensemble average of the transverse covariance matrix over many realizations is

$$\langle \mathbf{\Sigma}_\perp(t) \rangle = \langle \mathbf{\Delta}_\perp(t) \rangle + 2D_0 \langle \mathbf{\Lambda}_\perp(t) \rangle \equiv \sigma^2_{x_i}(t)\mathbf{I}, \tag{58}$$

where $\sigma^2_{x_i}(t)$ is the ensemble-averaged variance of the blob at time t in the i-direction transverse to the flow. As $\langle \mathbf{\Delta}_\perp(t) \rangle$ is constant for isotropic Darcy flow (as $F_{22}(t)$, $F_{33}(t)$ fluctuate without growth), and the asymptotic macrodispersion coefficients satisfy $D_0 + D^m_{ii} = \frac{1}{2}\lim_{t\to\infty} \frac{d}{dt}\sigma^2_{x_i}(t)$, then these coefficients are given as

$$D^m_{22} = D_0 \left(\left\langle \frac{m(0)}{v(0)} \right\rangle \langle v \rangle \left\langle \frac{1}{m} \right\rangle - 1 \right), \quad D^m_{33} = D_0 \left(\left\langle \frac{1}{v(0)m(0)} \right\rangle \langle v \rangle \langle m \rangle - 1 \right). \tag{59}$$

The ensemble averages of $m(0)$, $v(0)$ may be expressed as

$$\left\langle \frac{m(0)}{v(0)} \right\rangle = \sigma(m(0), 1/v(0)) + \langle m(0) \rangle \left\langle \frac{1}{v(0)} \right\rangle, \tag{60}$$

$$\left\langle \frac{1}{m(0)v(0)} \right\rangle = \sigma(1/m(0), 1/v(0)) + \left\langle \frac{1}{m(0)} \right\rangle \left\langle \frac{1}{v(0)} \right\rangle, \tag{61}$$

where $\sigma(a, b)$ denotes the covariance of a and b. The covariances $\sigma(m(0), 1/v(0))$, $\sigma(1/m(0), 1/v(0))$ are non-zero in statistically anisotropic media such as stratified media (where $m = v$ if the medium is heterogeneous only in the x_3 direction) and zero in statistically isotropic media (where the pdf of $\ln m$ is symmetric about zero). Under uniform injection conditions $\langle 1/v(0) \rangle = \langle 1/v \rangle$ and so the dispersion coefficients are

$$D^m_{22} = D_0 \left[\left(\sigma(m, 1/v) + \left\langle \frac{1}{v} \right\rangle \langle m \rangle \right) \langle v \rangle \left\langle \frac{1}{m} \right\rangle - 1 \right], \tag{62}$$

$$D^m_{33} = D_0 \left[\left(\sigma(1/m, 1/v) + \left\langle \frac{1}{v} \right\rangle \left\langle \frac{1}{m} \right\rangle \right) \langle v \rangle \langle m \rangle - 1 \right]. \tag{63}$$

For flux-weighted injection, the ensemble average $\langle 1/v(0) \rangle = 1/\langle v \rangle$, and so the dispersion coefficients are

$$D^m_{22} = D_0 \left[\left(\sigma(m, 1/v) + \frac{\langle m \rangle}{\langle v \rangle} \right) \langle v \rangle \left\langle \frac{1}{m} \right\rangle - 1 \right], \tag{64}$$

$$D^m_{33} = D_0 \left[\left(\sigma(1/m, 1/v) + \frac{1}{\langle v \rangle} \left\langle \frac{1}{m} \right\rangle \right) \langle v \rangle \langle m \rangle - 1 \right]. \tag{65}$$

For statistically isotropic media, the dispersion coefficients for uniform and flux-weighted injection protocols respectively simplify to

$$\text{uniform injection: } D_{22}^m = D_{33}^m = D_0\left(\left\langle \frac{1}{v}\right\rangle \langle v\rangle \langle m\rangle^2 - 1\right), \tag{66}$$

$$\text{flux-weighted injection: } D_{22}^m = D_{33}^m = D_0\left(\langle m\rangle^2 - 1\right). \tag{67}$$

Thus, transverse macrodispersion in statistically isotropic Darcy flow is controlled by the fluctuation of the distance between streamlines, as quantified by $\langle 1/v\rangle\langle v\rangle\langle m\rangle^2 \geqslant 1$ and $\langle m\rangle^2 \geqslant 1$ respectively for uniform and flux-weighted solute injection protocols. The somewhat surprising result (67) that transverse macrodispersion does not depend upon velocity fluctuations (when local dispersion D_0 is independent of velocity) under flux-weighted injection arises as the solute injection protocol exactly balances the contribution from subsequent velocity fluctuations. This behavior was also reported by Ye et al. (2015), who found transverse macrodispersion dispersion is zero for the radially symmetric case $m = 1$. Conversely, (66) shows that under uniform injection conditions, velocity fluctuations as well as fluctuations in m contribute to transverse dispersion. Typically, one would expect the macrodispersion coefficients for uniform and flux-weighted injection to converge with time due to growth of the solute plume dominating over the inlet conditions, however for statistically isotropic media these coefficients only fluctuate due to fluctuations in m and/or v, hence differences in the injection protocol persist for arbitrarily long times.

For statistically anisotropic but locally isotropic media, v and m are positively or negatively correlated due to the differences in correlation structure in the x_2 and x_3 directions. In this case, if the x_3 direction is defined to align with the direction of shortest correlation length of the conductivity field (which can be done due to non-uniqueness of the streamfunctions ψ_1, ψ_2), then $\sigma(m, 1/v) > 0$, $\sigma(1/m, 1/v) < 0$, $0 < \langle 1/m\rangle < 1 < \langle m\rangle$, and so from Equations 62–65, transverse macrodispersion dominates in the x_3 direction $\left(D_{33}^m > D_{22}^m\right)$ for both uniform and flux-weighted injection protocols. For both statistically isotropic and anisotropic media, the transverse macrodispersion coefficients both $D^m \to 0$ limit to zero in the limit of vanishing local dispersion, $D_0 \to 0$. Hence the kinematic constraints associated with these flows play a governing role in controlling solute transport in the regime of large Pèclet number. Conversely, if streamlines can diverge without bound (as is the case for locally anisotropic media), then transverse macrodispersion is non-zero in the case $D_0 \to 0$ as transverse deformation of the initial solute blob (as quantified by $|\boldsymbol{\Delta}_\perp(t)|$ grows exponentially with time). Similarly, in the presence of local dispersion is present, transverse macrodispersion is significantly amplified as $|\boldsymbol{\Lambda}_\perp(t)|$ also grows exponentially in time. Note that exponential growth of the plume does not persist as this is based upon first-order truncation of Equation 39 which breaks down at large times.

6.2. Numerical Analysis

To test the theoretical predictions given by Equation 67, we consider transverse macrodispersion in the presence of local dispersion in the model flow considered in Section 5 and track particles via the Pollock, Runge-Kutta and Pseudo-symplectic methods described in this section. As the cubic domain Ω is periodic, the streamlines of the unbounded flow $\mathbf{v}_\infty(\mathbf{x})$ are not representative of a random unbounded medium. To overcome this issue, we use a random re-injection protocol to construct aperiodic streamlines than span multiple domain lengths. Numerical simulation of transverse macrodispersion is performed by adding Gaussian noise to the various particle tracking methods (Pollock, Runge-Kutta and pseudo-symplectic) described in Section 5, with a grid resolution of $\Delta/\Delta_0 = 1$ for the Pollock method, and a tolerance of $\text{tol} = 10^{-4}$ for the Runge-Kutta method. From Equation 67, the transverse variance $\sigma_\perp^2(t)$ for this flow evolves with time as

$$\sigma_\perp^2(t) = 2\frac{\ell\langle v\rangle}{Pe}\langle m\rangle^2 t, \tag{68}$$

the parameters of which are determined by the model flow considered in Section 5. Figure 5a shows that the PDF of the Eulerian velocity magnitude v is well described by a Gamma distribution with scale parameter $\alpha \approx 0.022$ and index $\beta \approx 6.572$ (hence $\langle v\rangle = \alpha\beta \approx 0.1453$ and $\langle 1/v\rangle = 1/(\beta(\alpha - 1)) \approx 8.116$), and Figure 5b shows that $\ln m$ is normally distributed with zero mean and variance $\sigma_{\ln m}^2 \approx 0.1047$ (hence $\langle m\rangle^2 = \exp\left(\sigma_{\ln m}^2\right)$). As Equation 68 is based on a first-order expansion of the velocity field, it is only expected to hold over short periods $t < t_d$, where

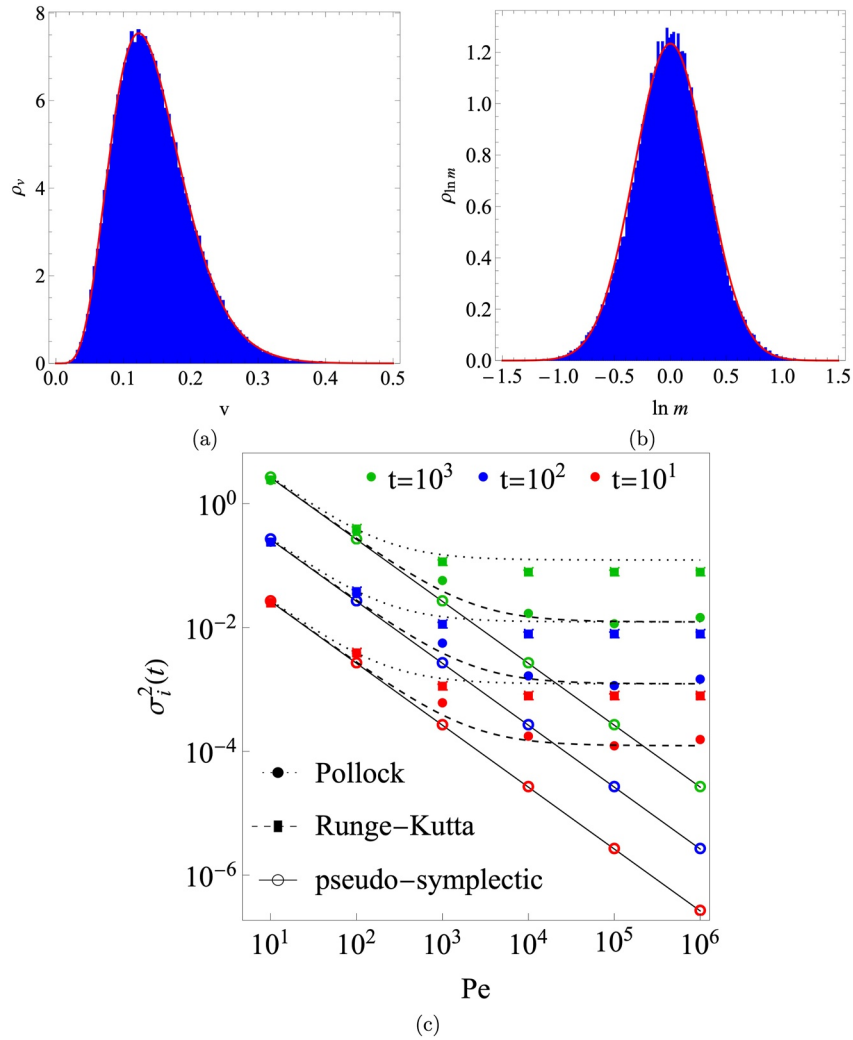

Figure 5. (a) PDF of v (blue area) and fitted Gamma distribution (red line). (b) PDF of $\ln m$ (blue area) and fitted normal distribution with zero mean (red line). (c) Evolution of transverse variance $\sigma_i^2(t)$ resulting from flux-weighted injection of a solute plume in the presence of local dispersion for various values of the Pèclet number Pe. Numerical values indicated by symbols are computed by adding Gaussian noise to the Pollock (solid squares), Runge-Kutta (solid circles) and pseudo-symplectic (open circles) particle tracking algorithms. Solid, dotted and dashed lines respectively indicate analytic predictions (69) of computed transverse macrodispersion for pseudo-symplectic, Runge-Kutta and Pollock algorithms. Solid lines also correspond to theoretical predictions given by Equation 68.

the diffusive timescale $t_d = \ell^2/D_0 = \ell Pe/\langle v\rangle$ corresponds to the diffusion of solute particles over one correlation length ℓ of the conductivity field. In the presence of particle tracking errors associated the computed transverse variance (68) is then

$$\sigma_\perp^2(t) = 2\frac{\ell\langle v\rangle}{Pe}\langle m\rangle^2 t + \sigma_x^2\frac{t}{\langle 1/v\rangle}, \tag{69}$$

where σ_x^2 is the average of the spatial errors for the Pollock and Runge-Kutta methods reported respectively in Figures 3c and 4b. A flux-weighted solute particle injection protocol is chosen over 10^5 distinct locations throughout the triply-periodic domain Ω, and ensemble averaging is performed over the resultant trajectories to compute transverse variance $\sigma_\perp^2(t)$. Figure 5c shows evolution of both the analytic and numerically computed transverse variance $\sigma_\perp^2(t)$ for different values of the Pèclet number Pe. Numerical results from the Pollock and Runge-Kutta methods over-predict transverse macrodispersion at large Pe due to particle tracking errors, which agrees well with the analytic estimate given by Equation 69. As the Pollock method for $\Delta/\Delta_0 = 1$ exhibits greater errors $\sigma_{x_1}^2$

than the Runge-Kutta method for tol = 10^{-4}, the Pollock method diverges at lower Pe. Figures 3c and 4b show that with decreasing grid resolution or increasing tolerance, predictions of transverse macrodispersion via the Pollock and Runge-Kutta methods diverges from the analytic solution at lower Pe. For moderate Pe, predictions of transverse macrodispersion via both of these methods converge toward the analytic solution (68). Conversely, Figure 5c shows that the pseudo-symplectic method agrees very well with the analytic prediction (68) for all Pe. These results highlight the need to exert caution when interpreting results from numerical schemes which do not explicitly preserve the Lagrangian kinematics of the underlying groundwater flow model.

7. Conclusions

The question of whether transverse macrodispersion exists in groundwater flow in the pure advection limit is contingent entirely upon the Lagrangian kinematics (topological complexity) of the flow field. This question is relevant for both physical systems and their mathematical models. As experimental studies show that all heterogeneous porous media exhibit non-zero transverse macrodispersion in the limit of large Péclet number *Pe* (Dagan, 1989; Gelhar, 1993), it is important to determine which mathematical models capture this behavior. In this study we address this problem by exploring the Lagrangian kinematics of various hydraulic conductivity models and associated numerical methods and their impacts on transverse macrodispersion. These findings reconcile several seemingly contradictory results in the literature and provide insights as to which classes of models are representative of physical groundwater flow and transport.

This kinematic constraint that 1D streamlines in a 2D domain cannot diverge was used by Attinger et al. (2004) to prove that all steady 2D flow models have zero asymptotic transverse macrodispersion in the absence of local dispersion. Conversely, 1D streamlines are free to wander in steady 3D flows and so may continually separate transversally, leading to non-zero asymptotic transverse macrodispersion. However, all steady 3D Darcy flows with a smooth and locally isotropic hydraulic conductivity are helicity-free (in that streamlines are everywhere orthogonal to vortex lines), which constrains the Lagrangian kinematics. In this study we show that all helicity-free flows admit a pair of streamfunctions which confine streamlines and render the flow topology equivalent to a steady 2D flow, and so prohibit transverse macrodispersion. We then rigorously prove that the asymptotic transverse macrodispersion coefficients for these flows are zero in the purely advective case.

It may be argued that a small amount of local dispersion is sufficient to overcome these kinematic constraints as the limit $\mathbf{D}_0 \to \mathbf{0}$ may be a *singular* limit, in that the fully resolved advection Equation 1 for vanishingly small $\mathbf{D}_0$ gives markedly different results for the advection only case $\mathbf{D}_0 = \mathbf{0}$. Certainly, for flows that exhibit chaotic advection (involving persistent exponential stretching of material elements), the ADE is singular with respect to vanishing diffusivity (Cerbelli et al., 2017), however this is not the case for non-chaotic flows such as steady locally isotropic Darcy flow, due to its helicity-free nature. Thus, the magnitude to which the evolution of a diffusive solute plume violates the kinematic constraints of isotropic Darcy flow scales as $|\mathbf{D}_0|$. Hence if solute transport is advection-dominated (i.e., $Pe \gg 1$), then the kinematic constraints of isotropic Darcy flow dominate evolution of the solute plume, and as shown by Equation 59 and the numerical results shown Figure 5, the macrodispersion coefficients scale linearly with molecular diffusivity in this regime.

In contrast to the findings outlined above, several studies have found that transverse macrodispersion is non-zero in steady state 3D isotropic Darcy flows, and so these observations warrant further discussion. Janković et al. (2003, 2009) and Di Dato, Fiori, et al. (2016); Di Dato, de Barros et al. (2016) find transverse macrodispersion occurs in steady 3D Darcy flow with non-smooth isotropic hydraulic conductivity fields. For these media the helicity is undefined (as is the velocity gradient) where the conductivity field is non-smooth, and so the kinematic constraints that are normally associated with these flows are relaxed over these regions. This allows streamlines to wander in an unconfined manner, leading to non-zero transverse macrodispersion.

Beaudoin and de Dreuzy (2013) also find transverse macrodispersion is non-zero in numerical studies of helicity-free isotropic Darcy flow. We show that these results may be attributed to the particle tracking methods employed in these studies that do not explicitly adhere to the kinematic constraints of these flows. We study this issue in further by performing numerical particle tracking in a steady 3D isotropic Darcy flow that is solved in terms of the underlying streamfunctions. There exist two sources of particle tracking error: one arises from using an velocity field representation that is not comprised of two streamfunctions, and another from numerical integration methods that don't preserve these streamfunctions along streamlines.

We examine the impact of the first error via a Pollock algorithm which is based upon the exact solution of streamlines based upon a linear interpolation of the velocities at cell faces. The impact of the second error is examine by using a Runge-Kutta algorithm to integrate streamlines from the exact velocity field based upon a pair of streamfunctions. We find that both algorithms generate particle trajectories that deviate from the true streamlines of the flow in a manner that mimics Brownian motion, and the Pollock algorithm introduces larger errors (that scale as grid size squared) than the Runge-Kutta errors (that scale with tolerance). For both methods, the apparent transverse macrodispersion asymptotes toward zero with increasing numerical accuracy, suggesting that the true transverse macrodispersion coefficients can be obtained via rigorous convergence studies. We also propose a novel *pseudo-symplectic* particle tracking method that is based on the streamfunction representation (14) of the Darcy equation, which ensures that the kinematic constraints associated with isotropic Darcy flow are conserved. As expected, this method predicts that transverse macrodispersion is zero in the purely advective limit.

We also develop a simple analytic model of transverse dispersion in the presence of local dispersion that corresponds to a first-order truncation of the local velocity field around a streamline. This analytic model agrees very well with numerical simulations based on the psuedo-symplectic method, but the Pollock and Runge-Kutta algorithms involve significant errors in the limit of large *Pe*. This model indicates that for helicity-free flows, transverse macrodispersion scales linearly with the magnitude of local dispersion, indicating transverse macrodispersion is regular in that it smoothly limits to zero in the limit of vanishing local dispersion. We show that for large *Pe*, transverse macrodispersion is controlled by variations in the distance between neighboring streamlines, and so the kinematic constraints inherent to isotropic Darcy flow govern solute transport in this regime. We also note that transverse macrodispersion in these flows scales linearly with the underlying isotropic dispersivity, which is consistent with non-singular dispersion for non-chaotic flows, that is, transverse macrodispersion smoothly limits to zero with vanishing local dispersivity. For statistically isotropic porous media, the transverse macrodispersion coefficients are also isotropic and their magnitude depends upon the solute injection protocol (uniform or flux-weighted). Conversely, statistically anisotropic but locally isotropic porous media results in anisotropic macrodispersion coefficients that also alter with injection protocols. We also show that locally anisotropic media results in non-zero transverse macrodispersion in the purely advective limit, and transverse dispersion is significantly faster that than for isotropic media when local dispersion is present.

In contrast to locally isotropic media, heterogeneous Darcy flow in porous media with a locally anisotropic conductivity field admits non-zero helicity and streamlines that can wander freely throughout the flow, leading to finite transverse macrodispersion in the purely advective limit. Indeed, several studies (Chaudhuri & Sekhar, 2005; Dartois et al., 2018; Neuman et al., 1987) have measured transverse macrodispersion arising from locally anisotropic media and found that it is significant larger than that for locally isotropic media. The advent of transverse macrodispersion in locally anisotropic porous media raises a conundrum in terms of upscaling of locally isotropic but statistically anisotropic Darcy flow to the block-scale, as the upscaled block-scale Darcy flow is now anisotropic and thus admits flows with non-zero helicity (Chiogna et al., 2015). This means that the fully resolved, locally isotropic Darcy flow does not permit transverse macrodispersion in the purely advective limit, but such behavior is possible under the upscaled anisotropic Darcy flow. The advent of novel phenomena at the block scale violates the coarse-graining principle that upscaling may only preserve or reduce information, hence such behavior at the block scale is spurious. This observation suggests that care must be exerted when upscaling groundwater flows, and calls for *kinematically-consistent* upscaling techniques that preserve the topology of the fully resolved Darcy flow. For locally isotropic Darcy flow, one such method involves upscaling on the basis of the streamfunctions $\psi_1(\mathbf{x})$, $\psi_2(\mathbf{x})$, such that the upscaled velocity field $\langle \mathbf{v}(\mathbf{x}) \rangle$ is defined as

$$\langle \mathbf{v}(\mathbf{x}) \rangle \equiv \nabla \langle \psi_1(\mathbf{x}) \rangle \times \nabla \langle \psi_2(\mathbf{x}) \rangle, \tag{70}$$

and so the streamfunction formulation (13) and associated kinematic constraints are preserved at the block scale. The development of a broader class of kinematically consistent upscaling methods is an open question that requires further investigation.

This result also raises an important fundamental question regarding the upscaling of porous media flow and transport from the pore to continuum scales. Pore-scale flow is described by the Navier-Stokes equations, which typically generate flows with non-zero helicity (even in the Stokes regime), leading to chaotic mixing (Lester et al., 2013, 2016) and non-zero transverse dispersion in the purely advective limit. Upscaling to the continuum scale typically involves the assumption of a smooth, locally isotropic conductivity field which generates

helicity-free flow, and the effects of pore-scale flow and transport are captured via the pore-scale transverse dispersion coefficient. However, the results above show that this assumption, which leads to zero transverse macrodispersion at the Darcy scale, must also persist at the block scale (if averaging is performed consistently, see below for further discussion). As experimental studies show that all heterogeneous media, exhibit non-zero transverse macrodispersion, these results call into question whether smooth isotropic conductivity fields can act as faithful representations of real heterogeneous porous media.

We also note that discontinuities in the hydraulic conductivity field should not occur when based upon volume averaging of the support volume. Instead, consider volume averaging near a planar conductivity discontinuity at the support scale. Volume averaging results in a harmonic average of conductivities in the direction normal to the planar discontinuity, and arithmetic averages in the directions parallel to the discontinuity, hence the resultant conductivity field is smooth and anisotropic.

These findings reinforce that an understanding of the Lagrangian kinematics admitted by specific groundwater flow models is necessary to properly interpret the results generated by these models. Furthermore, careful consideration must also be paid to the numerical schemes that are used to study these models, as some numerical methods can generate spurious transverse macrodispersion. Although this study primarily is focused on asymptotic dispersion, these findings are relevant to both the pre-asymptotic and asymptotic regimes.

Appendix A: Exact Transverse Macrodispersion Coefficients for General Streamfunctions

For the general case where $\overline{\mathbf{v}} = \overline{v}\hat{\mathbf{e}}_1$, the mean field components of the streamfunctions may be expressed via Equation 28 where $\overline{v} \equiv a_1 b_2 - a_2 b_1 \neq 0$. From Equation 13, the mean and fluctuating components of the velocity field are then explicitly

$$\overline{\mathbf{v}}(\mathbf{x}) = \mathbf{g}_1 \times \mathbf{g}_2 = \overline{v}\hat{\mathbf{e}}_1, \qquad \tilde{\mathbf{v}}(\mathbf{x}) = \nabla\tilde{\psi}_1(\mathbf{x}) \times \nabla\tilde{\psi}_2(\mathbf{x}) + \nabla\tilde{\psi}_1(\mathbf{x}) \times \mathbf{g}_2 - \nabla\tilde{\psi}_2(\mathbf{x}) \times \mathbf{g}_1, \tag{A1}$$

where $\mathbf{g}_i \equiv \nabla\overline{\psi}_i(\mathbf{x}) = a_i\hat{\mathbf{e}}_2 + b_i\hat{\mathbf{e}}_3$, $i = 1, 2$ and $\overline{v} \equiv |\overline{\mathbf{v}}| = a_1 b_2 - a_2 b_1$. We now show that the auxillary variables χ_2, χ_3 that are associated with the transverse macrodispersion coefficients D_{22}^m, D_{33}^m may be expressed directly in terms of the streamfunction fluctuations as

$$\chi_2(\mathbf{x}) = \frac{1}{\overline{v}}(b_1\tilde{\psi}_2(\mathbf{x}) - b_1\tilde{\psi}_1(\mathbf{x})), \tag{A2}$$

$$\chi_3(\mathbf{x}) = \frac{1}{\overline{v}}(a_2\tilde{\psi}_1(\mathbf{x}) - a_1\tilde{\psi}_2(\mathbf{x})), \tag{A3}$$

via substitution into Equation 7. For example, for $j = 2$ the LHS and RHS of Equation A2 are equivalent as

$$\begin{aligned}\mathbf{v}(\mathbf{x}) \cdot \nabla\chi_2(\mathbf{x}) &= \hat{\mathbf{e}}_1 \cdot (b_1\nabla\tilde{\psi}_2 - b_1\nabla\tilde{\psi}_1) + \frac{b_1}{\overline{v}}(\nabla\tilde{\psi}_1 \times \mathbf{g}_2) \cdot \nabla\tilde{\psi}_2 + \frac{b_2}{\overline{v}}(\nabla\tilde{\psi}_2 \times \mathbf{g}_1) \cdot \nabla\tilde{\psi}_1 \\ &= \hat{\mathbf{e}}_2 \cdot (\nabla\tilde{\psi}_1 \times \mathbf{g}_2) - \hat{\mathbf{e}}_2 \cdot (\nabla\tilde{\psi}_2 \times \mathbf{g}_1) + \hat{\mathbf{e}}_2 \cdot (\nabla\tilde{\psi}_1 \times \nabla\tilde{\psi}_2) \\ &= \tilde{\mathbf{v}} \cdot \hat{\mathbf{e}}_2 = \tilde{v}_2(\mathbf{x}),\end{aligned} \tag{A4}$$

and likewise for $j = 3$, $\mathbf{v}(\mathbf{x}) \cdot \nabla\chi_3(\mathbf{x}) = \tilde{v}_3(\mathbf{x})$. Substituting Equations A2 and A3 into Equation 4 yields the following expressions for the transverse macrodispersion coefficients

$$D_{22}^m = \langle\tilde{v}_2\chi_2\rangle = \langle b_2\hat{\mathbf{e}}_1 \cdot \nabla\tilde{\psi}_1 + b_1\hat{\mathbf{e}}_1 \cdot \nabla\tilde{\psi}_2 +\rangle, \tag{A5}$$

with a similar expression for D_{33}^m. Writing $\nabla\tilde{\psi}_1 \times \nabla\tilde{\psi}_2 = -\nabla \times \tilde{\psi}_2\nabla\tilde{\psi}_1$, then

$$D_{22}^m = -\left\langle \frac{1}{2}\frac{\partial\tilde{\psi}_1^2}{\partial x_1} - \tilde{\psi}_1\nabla \cdot (\tilde{\psi}_2\nabla\tilde{\psi}_1 \times \hat{\mathbf{e}}_2) \right\rangle \tag{A6}$$

$$= -\left\langle \nabla \cdot \left(\frac{\tilde{\psi}_1^2}{2}\hat{\mathbf{e}}_1 - (\tilde{\psi}_1\tilde{\psi}_2\nabla\tilde{\psi}_1 \times \hat{\mathbf{e}}_2) \right) \right\rangle \equiv \langle\nabla \cdot \mathbf{f}(\mathbf{x})\rangle, \tag{A7}$$

and substituting into Equation 3 yields

$$D_{22}^{m} = \lim_{V\to\infty} \frac{1}{V} \int_{V} \nabla \cdot \mathbf{f}(\mathbf{x}) d^3\mathbf{x} = \lim_{V\to\infty} \frac{1}{V} \oint_{\partial V} \mathbf{n} \cdot \mathbf{f}(\mathbf{x}) d^2\mathbf{x} = 0, \tag{A8}$$

as the values of $\mathbf{f}(\mathbf{x})$ are finite in the limit $|\mathbf{x}| \to \infty$. Similar arguments show that D_{33}^{m} is also zero.

Data Availability Statement

The computational data and codes for data analysis supporting this work are available upon request and as a Figshare repository at https://doi.org/10.25439/rmt.21314352.

Acknowledgments
The authors thank the reviewers for their constructive feedback which has improved the manuscript. M.D. acknowledges the support of the Spanish Research Agency (https://doi.org/10.13039/501100011033), Spanish Ministry of Science and Innovation and European Regional Development Fund "A way of making Europe" through Grants CEX2018-000794-S and Hydro-Pore PID2019-106887GB-C31. Open access publishing facilitated by RMIT University, as part of the Wiley - RMIT University agreement via the Council of Australian University Librarians.

References

Arnol'd, V. I. (1997). *Mathematical methods of classical mechanics* (2nd ed., Vol. 261). Springer.
Attinger, S., Dentz, M., & Kinzelbach, W. (2004). Exact transverse macro dispersion coefficients for transport in heterogeneous porous media. *Stochastic Environmental Research and Risk Assessment*, *18*(1), 9–15. https://doi.org/10.1007/s00477-003-0160-6
Bauer, R. D., Maloszewski, P., Zhang, Y. C., Meckenstock, R. U., & Griebler, C. (2008). Mixing-controlled biodegradation in a toluene plume—Results from two-dimensional laboratory experiments. *Journal of Contaminant Hydrology*, *96*(1–4), 150–168. https://doi.org/10.1016/j.jconhyd.2007.10.008
Bear, J. (1972). *Dynamics of fluids in porous media (no. 1)*. Dover.
Beaudoin, A., & de Dreuzy, J.-R. (2013). Numerical assessment of 3-D macrodispersion in heterogeneous porous media. *Water Resources Research*, *49*(5), 2489–2496. https://doi.org/10.1002/wrcr.20206
Beckie, R. (2001). A comparison of methods to determine measurement support volumes. *Water Resources Research*, *37*(4), 925–936. https://doi.org/10.1029/2000wr900366
Bouchaud, J.-P., & Georges, A. (1990). Anomalous diffusion in disordered media: Statistical mechanisms, models and physical applications. *Physics Reports*, *195*(4), 127–293. https://doi.org/10.1016/0370-1573(90)90099-n
Cerbelli, S., Giona, M., Gorodetskyi, O., & Anderson, P. D. (2017). Singular eigenvalue limit of advection-diffusion operators and properties of the strange eigenfunctions in globally chaotic flows. *The European Physical Journal Special Topics*, *226*(10), 2247–2262. https://doi.org/10.1140/epjst/e2017-70068-6
Chaudhuri, A., & Sekhar, M. (2005). Analytical solutions for macrodispersion in a 3d heterogeneous porous medium with random hydraulic conductivity and dispersivity. *Transport in Porous Media*, *58*(3), 217–241. https://doi.org/10.1007/s11242-004-6300-8
Chiogna, G., Cirpka, O. A., Rolle, M., & Bellin, A. (2015). Helical flow in three-dimensional nonstationary anisotropic heterogeneous porous media. *Water Resources Research*, *51*(1), 261–280. https://doi.org/10.1002/2014wr015330
Chiogna, G., Rolle, M., Bellin, A., & Cirpka, O. A. (2014). Helicity and flow topology in three-dimensional anisotropic porous media. *Advances in Water Resources*, *73*, 134–143. https://doi.org/10.1016/j.advwatres.2014.06.017
Cirpka, O. A., Chiogna, G., Rolle, M., & Bellin, A. (2015). Transverse mixing in three-dimensional nonstationary anisotropic heterogeneous porous media. *Water Resources Research*, *51*(1), 241–260. https://doi.org/10.1002/2014wr015331
Cirpka, O. A., Rolle, M., Chiogna, G., de Barros, F. P. J., & Nowak, W. (2012). Stochastic evaluation of mixing-controlled steady-state plume lengths in two-dimensional heterogeneous domains. *Journal of Contaminant Hydrology*, *138*(22–39), 22–39. https://doi.org/10.1016/j.jconhyd.2012.05.007
Cole, C. R., & Foote, H. P. (1990). Multigrid methods for solving multiscale transport problems. In J. H. Cushman (Ed.), *Dynamics of fluids in hierarchical porous media*. Academic Press Limited.
Dagan, G. (1987). Theory of solute transport by groundwater. *Annual Review of Fluid Mechanics*, *19*(1), 183–213. https://doi.org/10.1146/annurev.fl.19.010187.001151
Dagan, G. (1989). *Flow and transport in porous formations*. Springer.
Dagan, G. (1994). An exact nonlinear correction to transverse macrodispersivity for transport in heterogeneous formations. *Water Resources Research*, *30*(10), 2699–2705. https://doi.org/10.1029/94wr00904
Dartois, A., Beaudoin, A., & Huberson, S. (2018). Impact of local diffusion on macroscopic dispersion in three-dimensional porous media. *Comptes Rendus Mecanique*, *346*(2), 89–97. https://doi.org/10.1016/j.crme.2017.12.012
de Barros, F. P. J., Dentz, M., Koch, J., & Nowak, W. (2012). Flow topology and scalar mixing in spatially heterogeneous flow fields. *Geophysical Research Letters*, *39*(8). https://doi.org/10.1029/2012gl051302
Di Dato, M., de Barros, F. P. J., Fiori, A., & Bellin, A. (2016). Effects of the hydraulic conductivity microstructure on macrodispersivity. *Water Resources Research*, *52*(9), 6818–6832. https://doi.org/10.1002/2016wr019086
Di Dato, M., Fiori, A., Chiogna, G., de Barros, F. P. J., & Bellin, A. (2016). Impact of the spatial structure of the hydraulic conductivity field on vorticity in three-dimensional flows. *Proceedings of the Royal Society A*, *472*(2187), 20150730. https://doi.org/10.1098/rspa.2015.0730
Domenico, P. A., & Palciauskas, V. V. (1982). Alternative boundaries in solid waste management. *Ground Water*, *20*(3), 303–311. https://doi.org/10.1111/j.1745-6584.1982.tb01351.x
Dykaar, B. B., & Kitanidis, P. K. (1992). Determination of the effective hydraulic conductivity for heterogeneous porous media using a numerical spectral approach: 1. Method. *Water Resources Research*, *28*(4), 1155–1166. https://doi.org/10.1029/91wr03084
Gelhar, L. (1993). *Stochastic subsurface hydrology*. Prentice-Hall.
Gelhar, L., & Axness, C. (1983). Three-dimensional stochastic analysis of macrodispersion in aquifers. *Water Resources Research*, *19*(1), 161–180. https://doi.org/10.1029/wr019i001p00161
Greywall, M. S. (1993). Streamwise computation of three-dimensional flows using two stream functions. *Journal of Fluids Engineering*, *115*(2), 233–238. https://doi.org/10.1115/1.2910129
Guin, J. A., Kessler, D. P., & Greenkorn, R. A. (1972). The dispersion tensor in anisotropic porous media. *Industrial & Engineering Chemistry Fundamentals*, *11*(4), 477–482. https://doi.org/10.1021/i160044a008
Holm, D. D., & Kimura, Y. (1991). Zero-helicity Lagrangian kinematics of three-dimensional advection. *Physics of Fluids A: Fluid Dynamics*, *3*(5), 1033–1038. https://doi.org/10.1063/1.858083

Janković, I., Fiori, A., & Dagan, G. (2003). Flow and transport in highly heterogeneous formations: 3. Numerical simulations and comparison with theoretical results. *Water Resources Research*, *39*(9), 1268. https://doi.org/10.1029/2002wr001721

Janković, I., Steward, D. R., Barnes, R. J., & Dagan, G. (2009). Is transverse macrodispersivity in three-dimensional groundwater transport equal to zero? A counterexample. *Water Resources Research*, *45*(8), W08415. https://doi.org/10.1029/2009wr007741

Kraichnan, R. H. (1961). Dynamics of nonlinear stochastic systems. *Journal of Mathematical Physics*, *2*(1), 124–148. https://doi.org/10.1063/1.1724206

Le Borgne, T., Dentz, M., & Carrera, J. (2008). Lagrangian statistical model for transport in highly heterogeneous velocity fields. *Physical Review Letters*, *101*(9), 090601. https://doi.org/10.1103/physrevlett.101.090601

Lester, D. R., Bandopadhyay, A., Dentz, M., & Le Borgne, T. (2019). Hydrodynamic dispersion and Lamb surfaces in Darcy flow. *Transport in Porous Media*, *130*(3), 903–922. https://doi.org/10.1007/s11242-019-01346-3

Lester, D. R., Dentz, M., Bandopadhyay, A., & Borgne, T. L. (2022). Fluid deformation in isotropic Darcy flow. *Journal of Fluid Mechanics*, *945*, A18. https://doi.org/10.1017/jfm.2022.556

Lester, D. R., Dentz, M., Bandopadhyay, A., & Le Borgne, T. (2021). The kinematics of three-dimensional Darcy flow. *Journal of Fluid Mechanics*, *918*, A27. https://doi.org/10.1017/jfm.2021.362

Lester, D. R., Dentz, M., & Le Borgne, T. (2016). Chaotic mixing in three-dimensional porous media. *Journal of Fluid Mechanics*, *803*, 144–174. https://doi.org/10.1017/jfm.2016.486

Lester, D. R., Metcalfe, G., & Trefry, M. G. (2013). Is chaotic advection inherent to porous media flow? *Physical Review Letters*, *111*(17), 174101. https://doi.org/10.1103/physrevlett.111.174101

McComb, W. D. (1990). *The physics of fluid turbulence*. Clarendon.

Moffatt, H. K. (1969). The degree of knottedness of tangled vortex lines. *Journal of Fluid Mechanics*, *1*, 117–129. https://doi.org/10.1017/s0022112069000991

Moffatt, H. K., & Tsinober, A. (1992). Helicity in laminar and turbulent flow. *Annual Review of Fluid Mechanics*, *24*(1), 281–312. https://doi.org/10.1146/annurev.fl.24.010192.001433

Moreau, J. J. (1961). Constantes d'un îlot tourbillonnaire en fluide parfait barotrope. *Comptes rendus hebdomadaires des séances de l'Académie des sciences*, *252*, 2810–2812.

Nédélec, J. C. (1980). Mixed finite elements in R^3. *Numerical Mathematics*, *35*(3), 315–341. https://doi.org/10.1007/bf01396415

Neuman, S. P. (1993). Eulerian-Lagrangian theory of transport in space-time nonstationary velocity fields: Exact nonlocal formalism by conditional moments and weak approximation. *Water Resources Research*, *29*(3), 633–645. https://doi.org/10.1029/92wr02306

Neuman, S. P., Winter, C. L., & Newman, C. M. (1987). Stochastic theory of field-scale Fickian dispersion in anisotropic porous media. *Water Resources Research*, *23*(3), 453–466. https://doi.org/10.1029/wr023i003p00453

Neuman, S. P., & Zhang, Y.-K. (1990). A quasi-linear theory of non-Fickian and Fickian subsurface dispersion: 1. Theoretical analysis with application to isotropic media. *Water Resources Research*, *26*(5), 887–902. https://doi.org/10.1029/wr026i005p00887

Pollock, D. W. (1988). Semianalytical computation of path lines for finite-difference models. *Groundwater*, *26*(6), 743–750. https://doi.org/10.1111/j.1745-6584.1988.tb00425.x

Raviart, P. A., & Thomas, J. M. (1977). A mixed finite element method for second order elliptic problems. In I. Galligani & E. Magenes (Eds.), *Mathematical aspects of the finite element method* (Vol. 606, pp. 292–315). Springer-Verlag.

Ravu, B., Rudman, M., Metcalfe, G., Lester, D. R., & Khakhar, D. V. (2016). Creating analytically divergence-free velocity fields from grid-based data. *Journal of Computational Physics*, *323*(Supplement C), 75–94. https://doi.org/10.1016/j.jcp.2016.07.018

Rubin, Y., & Gómez-Hernández, J. J. (1990). A stochastic approach to the problem of upscaling of conductivity in disordered media: Theory and unconditional numerical simulations. *Water Resources Research*, *26*(4), 691–701. https://doi.org/10.1029/wr026i004p00691

Rubin, Y., Sun, A., Maxwell, R., & Bellin, A. (1999). The concept of block-effective macrodispersivity and a unified approach for grid-scale- and plume-scale-dependent transport. *Journal of Fluid Mechanics*, *395*, 161–180. https://doi.org/10.1017/s0022112099005868

Sanz-Serna, J. M. (1992). Symplectic integrators for Hamiltonian problems: An overview. *Acta Numerica*, *1*, 243–286. https://doi.org/10.1017/s0962492900002282

Schwarze, H., Jaekel, U., & Vereecken, H. (2001). Estimation of macrodispersion by different approximation methods for flow and transport in randomly heterogeneous media. *Transport in Porous Media*, *43*(2), 265–287. https://doi.org/10.1023/a:1010771123844

Sposito, G. (1994). Steady groundwater flow as a dynamical system. *Water Resources Research*, *30*(8), 2395–2401. https://doi.org/10.1029/94wr01328

Sposito, G. (1997). On steady flows with Lamb surfaces. *International Journal of Engineering Science*, *35*(3), 197–209. https://doi.org/10.1016/s0020-7225(96)00084-5

Sposito, G. (2001). Topological groundwater hydrodynamics. *Advances in Water Resources*, *24*(7), 793–801. https://doi.org/10.1016/s0309-1708(00)00077-4

Ye, Y., Chiogna, G., Cirpka, O. A., Grathwohl, P., & Rolle, M. (2015). Enhancement of plume dilution in two-dimensional and three-dimensional porous media by flow focusing in high-permeability inclusions. *Water Resources Research*, *51*(7), 5582–5602. https://doi.org/10.1002/2015wr016962

Yoshida, Z. (2009). Clebsch parameterization: Basic properties and remarks on its applications. *Journal of Mathematical Physics*, *50*(11), 113101. https://doi.org/10.1063/1.3256125

Zhang, Y.-K., & Neuman, S. P. (1990). A quasi-linear theory of non-Fickian and Fickian subsurface dispersion: 2. Application to anisotropic media and the borden site. *Water Resources Research*, *26*(5), 903–913. https://doi.org/10.1029/wr026i005p00903

Zijl, W. (1986). Numerical simulations based on stream functions and velocities in three—Dimensional groundwater flow. *Journal of Hydrology*, *85*(3), 349–365. https://doi.org/10.1016/0022-1694(86)90065-x